Global Biogeochemical Cycles

RESEARCH ARTICLE
10.1029/2020GB006633

Key Points:

- CO_2 uptake in lead waters is determined using water-atmosphere and ice-atmosphere flux measurements from an on-ice mast
- The wind-speed dependent gas transfer velocity in the lead is suppressed by 30% relative to the open ocean
- Dependent on choice of footprint model, k varies with fetch, hence polar ocean carbon uptake estimates should incorporate lead width data

Supporting Information:

- Supporting Information S1

Correspondence to:
J. Prytherch,
john.prytherch@misu.su.se

Citation:
Prytherch, J., & Yelland, M. J. (2021). Wind, convection and fetch dependence of gas transfer velocity in an Arctic sea-ice lead determined from eddy covariance CO_2 flux measurements. *Global Biogeochemical Cycles*, *35*, e2020GB006633. https://doi.org/10.1029/2020GB006633

Received 15 APR 2020
Accepted 31 DEC 2020

Wind, Convection and Fetch Dependence of Gas Transfer Velocity in an Arctic Sea-Ice Lead Determined From Eddy Covariance CO_2 Flux Measurements

J. Prytherch[1] and M. J. Yelland[2]

[1]Department of Meteorology, Stockholm University, Stockholm, Sweden, [2]Marine Physics and Ocean Climate, National Oceanography Centre, Southampton, UK

Abstract The air-water exchange of trace gases such as CO_2 is usually parameterized in terms of a gas transfer velocity, which can be derived from direct measurements of the air-sea gas flux. The transfer velocity of poorly soluble gases is driven by near-surface ocean turbulence, which may be enhanced or suppressed by the presence of sea ice. A lack of measurements means that air-sea fluxes in polar regions, where the oceanic sink of CO_2 is poorly known, are generally estimated using open-ocean transfer velocities scaled by ice fraction. Here, we describe direct determinations of CO_2 gas transfer velocity from eddy covariance flux measurements from a mast fixed to ice adjacent to a sea-ice lead during the summer-autumn transition in the central Arctic Ocean. Lead water CO_2 uptake is determined using flux footprint analysis of water-atmosphere and ice-atmosphere flux measurements made under conditions (low humidity and high CO_2 signal) that minimize errors due to humidity cross-talk. The mean gas transfer velocity is found to have a quadratic dependence on wind speed: $k_{660} = 0.179\ U_{10}{}^2$, which is 30% lower than commonly used open-ocean parameterizations. As such, current estimates of polar ocean carbon uptake likely overestimate gas exchange rates in typical summertime conditions of weak convective turbulence. Depending on the footprint model chosen, the gas transfer velocities also exhibit a dependence on the dimension of the lead, via its impact on fetch length and hence sea state. Scaling transfer velocity parameterizations for regional gas exchange estimates may therefore require incorporating lead width data.

Plain Language Summary Polar oceans absorb large amounts of carbon dioxide from the atmosphere, but there is a lot of uncertainty over exactly how much is taken up. The amount the oceans absorb depends on both the concentration of carbon dioxide in the water, and the rate of gas exchange between the ocean and the atmosphere. This rate itself depends mostly on wind speed. In sea ice-regions, which even in winter have some areas of open water, the gas exchange rate is often estimated by using an ocean gas exchange rate, multiplied by the fraction of the sea-ice area, that is, open water. However, there are very few measurements of the gas exchange rate in sea-ice areas, and there is an on-going debate about whether the sea ice itself increases or decreases the exchange rate. Here, direct measurements of the gas exchange rate were made in an area of water surrounded by sea ice in the Arctic during summer and the beginning of autumn. The measured gas exchange rate was lower than typical ocean rates, suggesting that the absorption of carbon dioxide by polar oceans has previously been overestimated.

1. Introduction

Polar oceans are important to the global ocean-atmosphere carbon cycle as major sinks. The Arctic Ocean accounts for approximately 3% of global ocean area, and is estimated to have 5%–14% of the net global ocean carbon uptake, for example, 66–199 Tg (Tg = 10^{12} g) C year^{-1} (Bates & Mathis, 2009); 166 ± 60 Tg C year^{-1} (MacGilchrist et al., 2014); 180 ± 130 Tg C year^{-1} (Yasunaka et al., 2018). The net Southern Ocean carbon flux is likely smaller due to the balance of strong summer uptake with strong winter emissions, but sparse sampling results in large uncertainty: Uptake for oceans south of 50°S (14% of the global ocean surface area) was estimated as 50 Tg C year^{-1} (Takahashi et al., 2009), while a more recent estimate for waters south of 60°S was approximately 130 Tg C year^{-1} (Woolf et al., 2019).

Most estimates of polar ocean carbon uptake utilize collations of ship and buoy observations of the partial pressure of CO_2 in seawater, pCO_2w, such as the Surface Ocean CO_2 Atlas (SOCAT) version 4 (Bakker

et al., 2016). For sea-ice areas, air-sea flux estimates derived from pCO_2w observations are scaled by the fraction of open water within the sea-ice area, either linearly (e.g., Bates & Mathis, 2009; Takahashi et al., 2009) or by incorporating a parameterization that estimates a flux larger than that from a linear scaling with open water fraction due to physical forcings from the sea ice itself (Yasunaka et al., 2018).

For a poorly soluble trace gas such as CO_2, the flux across an air-water interface, F_c, is often represented as a product of the air-water fugacity or partial-pressure difference, ΔpCO_2; the aqueous-phase solubility of the gas, $K0$; and the transfer coefficient, or transfer velocity, k:

$$F_c = k\, K0\, \Delta pCO_2 \tag{1}$$

The transfer velocity represents the interfacial turbulent processes on the water side that control the rate of exchange and that are challenging to measure directly (e.g., Jähne et al., 1987; Wanninkhof et al., 2009). Gas transfer velocity is thus typically parameterized using more easily measurable variables, most commonly wind speed. Despite recent progress, the greatest source of uncertainty in determining the carbon uptake by the global oceans remains the uncertainty in the form (quadratic or cubic) of the gas transfer parameterization (Woolf et al., 2019). Over the ocean, the most widely used parameterizations have a quadratic dependence on wind speed (e.g., Ho et al., 2006; Nightingale et al., 2000; Wanninkhof et al., 2014, hereafter W14) but there remains uncertainty in determining k, both at low and moderate wind speeds due to the suppression of near-surface turbulence by surfactants (e.g., Salter et al., 2011), and at higher wind speeds due to the uncertain influence of bubble-mediated exchange and wave forcing (e.g., McGillis et al., 2001; Woolf, 2005). Some progress has been made incorporating sea state into gas transfer parameterizations but there remain significant challenges due to limited data and an incomplete understanding of the physical mechanisms involved (Blomquist et al., 2017; Brumer et al., 2017).

Over lakes, indirect estimates of gas transfer velocity from dual tracer experiments determined lower wind-speed dependence than for the open ocean (Cole & Caraco, 1998; MacIntyre et al., 2010; Wanninkhof, 1992). Convection-driven turbulent mixing resulting from surface buoyancy flux has been observed to enhance gas transfer in lakes (MacIntyre et al., 2010): in small lakes (<10 ha) at latitudes <60°, it was determined to be the dominant driver of gas transfer (Read et al., 2012). The gas transfer velocity has also been found to depend on both the size and shape of the lakes (Vachon & Prairie, 2013).

In sea-ice regions, there remains uncertainty in air-water gas transfer rates due to both lack of measurements and the influence of the sea ice itself on near-surface turbulence. Ship-based determinations of k using direct eddy covariance (EC) flux measurements in the Arctic (Prytherch et al., 2017) and Antarctic (Butterworth & Miller, 2016a) marginal ice zones and pack ice found an approximately linear scaling of k with open water fraction. Observations from acoustic Doppler profile instruments mounted on floating drifters close to sea ice have shown suppressed near-surface turbulent dissipation rates, a proxy for turbulent mixing, relative to open ocean measurements, presumably due to attenuation of the wave field by the sea ice (Zippel & Thomson, 2016). Early estimates of k using radon isotope-deficit showed, in ice concentrations greater than 70%, an enhancement of k above that expected from a linear scaling with open water fraction (Fanning & Torres, 1991). Subsequent experiments using this method have shown both suppressions (Rutgers van der Loeff et al., 2014) and enhancements (Loose et al., 2017) of k relative to a linear scaling. The k estimates reported by Loose et al. (2017) showed only a weak dependence on wind speed, and the authors surmised that other kinetics were driving the gas exchange within the marginal ice zone and pack ice. Such forcing has been hypothesized to result from a number of physical mechanisms impacting the interfacial mixing, including shear between floating ice and the underlying water and form drag on the wind from ice edges (Loose et al., 2014), conclusions supported by laboratory measurements (Loose et al., 2009; Lovely et al., 2015). For low ice concentrations (<60%) and moderate ice drift velocity (ice/wind velocity ratio > 0.02), this additional forcing is predicted to be larger than any suppression of gas transfer resulting from wave field attenuation, whilst for higher ice concentrations or lower ice drift velocity, the gas transfer suppression is equal to or greater than the enhancement, resulting in a linear or lower scaling with open water fraction (Bigdeli et al., 2018).

Sea ice itself is known to be permeable to salt and gases via brine channels (Gosink et al., 1976) and drives physical and biogeochemical processes such as carbonate crystal formation and brine exclusion that affect

CO_2 concentrations in the underlying water (e.g., L. A. Miller, Carnat, et al., 2011). Ice-atmosphere fluxes may make a large contribution to the net carbon flux in polar regions (Delille et al., 2014). Varying CO_2 partial pressure in brines is thought to explain the range of sea ice-atmosphere CO_2 fluxes observed in both spring-summer (Delille et al., 2014; Geilfus et al., 2015, 2012; Nomura et al., 2013; Sievers et al., 2015) and winter seasons (L. A. Miller, Papakyriakou, et al., 2011). The observed flux is primarily dependent on the surface temperature (Delille et al., 2014; Geilfus et al., 2012) and on the snow conditions. Snow cover is generally shown to reduce the flux (e.g., Geilfus et al., 2012), with snow depth greater than 9 cm observed to block exchange (Nomura et al., 2010) and superimposed ice layers reduce or even entirely block the flux (Geilfus et al., 2012, 2015). On summer sea ice, there can also be a large flux into melt ponds due to the undersaturation of CO_2 in the melt waters. This flux is typically short lived ($<\sim$ 1 week) as the shallow melt waters rapidly equilibrate with the atmosphere following their formation, though ongoing melt can maintain a smaller undersaturation (Geilfus et al., 2015).

EC measurement of trace gas flux, combined with measurement of air and water gas concentrations and solubility enables k to be directly determined on time scales of order 30 min and spatial scales on the order of 100 m–1 km. Whilst EC CO_2 flux measurement has been long-established in terrestrial settings, they have proved challenging in marine conditions because of the typically much smaller CO_2 flux and the difficult measurement environment. Recent developments in instrumentation and measurement techniques, particularly the use of air-drying to reduce the water vapor cross-sensitivity apparent in infrared absorption-based CO_2 measurements (e.g., Blomquist et al., 2014; S. D. Miller et al., 2010) have improved agreement between k determined from EC and from other methods.

There is a well-known (see e.g., the summary by Butterworth & Else, 2018) disparity in the magnitude of sea ice-atmosphere CO_2 fluxes as observed by enclosure or chamber-based methods (L. A. Miller et al., 2015) and EC. The flux measured using chamber-based techniques is typically in the range -5 to $+2$ mmol m^{-2} day^{-1} (here a positive flux value represents a flux from the surface to the atmosphere; Delille et al., 2014; Geilfus et al., 2012, 2015; Nomura et al., 2010, 2013) whereas the flux determined from EC has a much larger range and variability, with magnitudes often in excess of 50 mmol m^{-2} day^{-1} (e.g., Else et al., 2011; Miller et al., 2011; Sievers et al., 2015). This may result from the relatively low sensitivity and cold temperature biases (Burba et al., 2008) of the open-path EC instrumentation (Butterworth & Else, 2018). More recent EC measurements using closed path instrumentation reported fluxes of 1.75 ± 5 mmol m^{-2} day^{-1} from snow-covered ice, in broad agreement with chamber flux measurements made close by (Sievers et al., 2015). EC flux measurements using a closed path system with airstream drying also measured low fluxes, averaging -0.03 mmol m^{-2} day^{-1} in spring with full ice cover, and -2.9 mmol m^{-2} day^{-1} during the summer ice breakup when the surface was a mixture of water and ice (Butterworth & Else, 2018). In contrast, measurements during the spring season from collocated open-path instruments measured fluxes several orders of magnitude higher.

Here we report direct determination of gas transfer velocities in an open lead close to the North Pole during summer and autumn in 2018. The gas transfer velocity is determined from EC measurement of CO_2 fluxes between both the lead waters and atmosphere, and between the sea-ice surface and atmosphere, using a flux footprint analysis. The dependence of the gas transfer velocity on wind speed, fetch and buoyancy is determined and the implications discussed.

2. Materials and Methods

2.1. Expedition

The Arctic Ocean 2018 expedition was focused on Arctic clouds, the sources of cloud condensation nuclei and ice nucleating particles in the central Arctic Ocean, and the interactions of clouds and sea ice. The expedition, based on the icebreaker *Oden*, departed Longyearbyen on August 1, 2018 and transited north into the ice pack. On August 13, *Oden* moored to an ice floe at 89.6°N 40°E. The ice floe was approximately 0.8×1.5 km in size, and surrounded by dense pack ice as well as some lead systems. Instrumentation was deployed on the ice floe at several different locations for a period of four weeks. *Oden* drifted with the ice floe, occasionally repositioning with changing wind direction to maintain winds onto the bow for the pur-

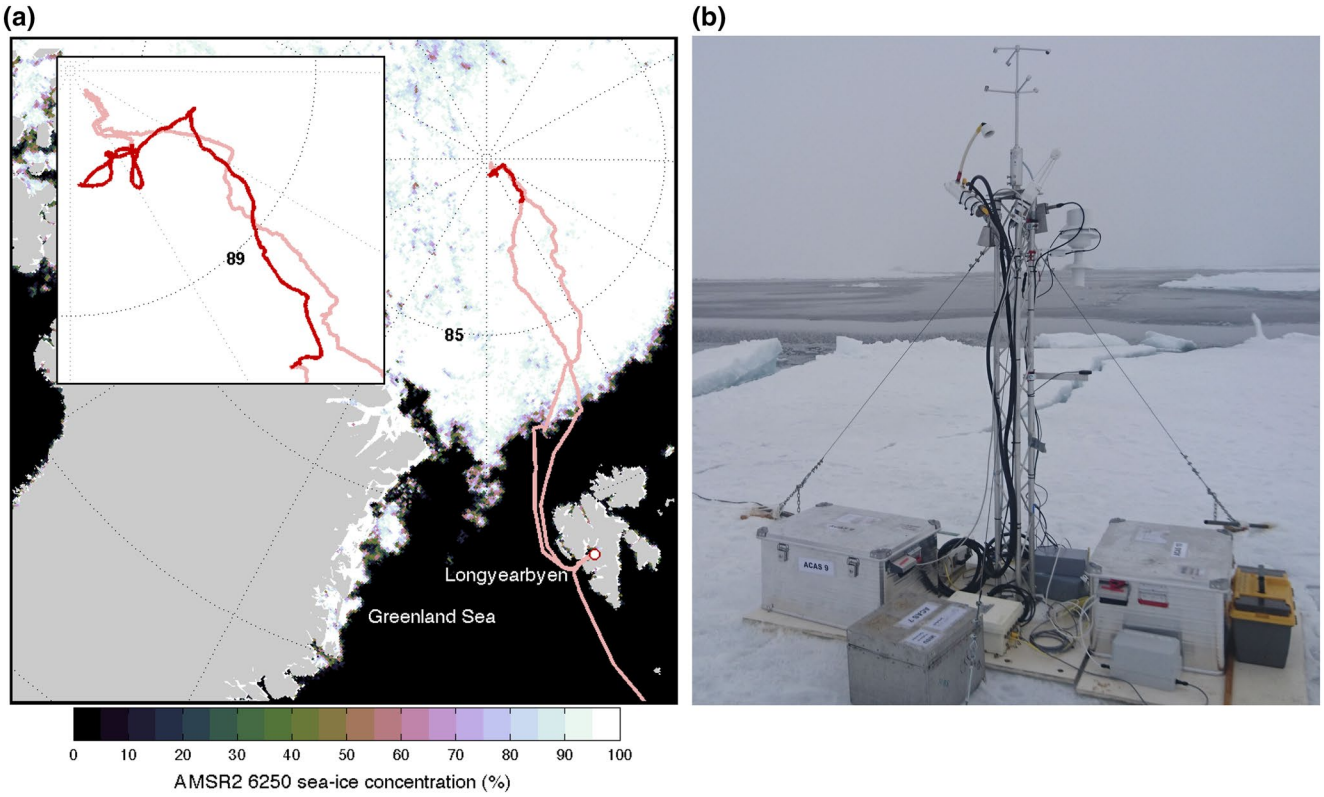

Figure 1. (a) Arctic Ocean 2018 expedition track, with the ice camp portion of the expedition highlighted (darker red). Sea-ice concentration (AMSR2 6250 satellite passive microwave measurement, Spreen et al., 2008; ASI 5 sea-ice algorithm) is shown for September 1, 2018. (b) The open lead mast on August 18, 2018. The surface water pCO_2w sensor is positioned ~3 m out into the lead to the left of frame.

poses of measurements made onboard the ship. The ice camp lasted until late on September 14, 2019, when *Oden* departed the ice floe at 88.49°N 36.8°E, returning to Longyearbyen on September 20 (Figure 1a). In addition to the measurements made on the ice floe, a wide variety of atmospheric and oceanographic measurements were made onboard *Oden* during both the ice camp and the transits. Relevant to the results here are a Seabird TSG measuring water temperature and salinity at 1 Hz on *Oden's* pumped underway line that draws from a depth of 8 m, and the downwelling short- and long-wave radiation measurements made using gymbal-mounted Eppley Laboratory PSP and PIR radiometers. These sensors were checked for ice buildup at regular intervals each day.

2.2. Open Lead Mast

A measurement site was located adjacent to a large lead system. This open lead site was on the far side of the ice floe from *Oden's* mooring, approximately 1.5 km distant from the ship. Instrumentation at this site was primarily concerned with processes occurring within, at or above the surface of the lead water. A small hut (~3 × 3 × 2 m) was constructed for storage and shelter and serves as a reference point in the moving sea-ice environment. A 2 m high meteorological mast (Figure 1b) was installed on August 16, ~140 m from the hut and most of the other measurement systems and ~6 m from the ice edge at the lead.

The three-dimensional wind vector and sonic temperature was measured with a METEK uSonic-3 heated sonic anemometer. Density of CO_2 and H_2O as well as air pressure were measured by both a LI-COR 7200 closed-path infrared gas analyzer (IRGA) and a LI-COR 7500 open-path IRGA. The closed-path IRGA derives dry air mole fractions from the density measurements using internal measurements of pressure, temperature, and humidity. This instrumentation all measured at 20 Hz. The measurement volume of the

uSonic-3 was at a height of 2.55 m above the ice surface, with the inlet for the closed-path IRGA 0.25 m below the anemometer, and the measurement volume of the open-path IRGA 0.45 m below the anemometer.

Also positioned on the mast were a Heitronics KT15. IIP infrared temperature sensor. The measurement point was focused on lead water ~5 m from the ice edge closest to the mast. The sensor measures *Ts*, the skin temperature of the water or ice, at 1 Hz. An aspirated temperature and humidity sensor measured air temperature (*Ta*) and relative humidity (RH) at a height above the ice of 2 m. A GPS unit at the mast determined location and ice drift velocity. A Pro Oceanus CO_2-Pro CV membrane equilibration sensor was deployed beneath a float in the lead waters closest to the mast ~3 m from the ice edge and at 0.5 m depth, measuring pCO_2w, the partial pressure of CO_2 in seawater. The CO_2-Pro CV was removed on September 9 due to heavy ice formation at its location.

Restrictions imposed to facilitate aerosol measurements onboard *Oden* and on the ice floe meant that all power at the open lead site came from batteries. The meteorological mast instrumentation was powered by six 12V batteries, which were exchanged on a daily basis. Data were logged at the mast, and backups taken daily. The mast was in operation for 28 days from August 16 to September 12, when the last data backup was taken at 20:00 UTC. In the early hours of September 13, moving ice destroyed the mast and the equipment installed there.

2.3. Data Processing

2.3.1. Meteorology and Fluxes

The fast response (20 Hz) measurements are divided into flux periods of 30-min duration. For each flux period, a double rotation is used to rotate the winds into the streamline (Wilczak et al., 2001). The momentum flux τ, and friction velocity are determined from the covariance of the fluctuations of the horizontal along-, cross- (u', v') and vertical-wind (w') components as:

$$u_* = \left(\tau \,/\, \rho\right)^{1/2} = \left(\overline{u'w'}^2 + \overline{v'w'}^2\right)^{1/4}. \tag{2}$$

where ρ is the mean air density, ' indicates a fluctuation from the mean value, and an overbar indicates a mean. The mean wind speed, U is adjusted to a height of 10 m using a log profile

$$U_{10} = U + u_* \log\left(10 \,/\, z_u\right) / \kappa \tag{3}$$

where z_u is the wind measurement height (2.55 m) and κ is the von Karman constant (here set as 0.4). In the summer conditions that comprise the majority of the data here, the air and surface temperatures are similar, and applying a stability adjustment (Andreas et al., 2010) to the U_{10} values results in a mean absolute change of approximately 1%. There is uncertainty in the applicability of similarity-theory based stability corrections in heterogeneous sea-ice regions (e.g., Lupkes et al., 2012). Hence in the following results we use U_{10} without an additional stability adjustment. Following linear detrending of the time series for each flux period, the kinematic flux, E_x of a scalar quantity x is determined as:

$$E_x = \overline{x'w'} \tag{4}$$

and the cospectra C_{xw} is determined from the same measurements. For CO_2, the flux is calculated from c, the dry mole fraction of CO_2 measured by the closed-path IRGA with units of ppm m s^{-1}. The dynamic flux, F_c (units of mmols m^{-2} day^{-1}) is determined using ρ_a, the dry air density and the molecular weight. The sensible heat flux is determined from the sonic temperature, t_{son} following correction for side wind path lengthening (van Dijk et al., 2004). Humidity is corrected for in the sensible heat flux calculation using a bulk estimate of the latent heat flux (Smith, 1988) following Persson et al. (2005). Fast response H_2O density measurements from the open-path IRGA are corrected for density effects (Webb et al., 1980) on a point-by-point basis following S. D. Miller et al. (2010, 2004). The resulting humidity mixing ratio is used to

determine the latent heat flux, F_l. Throughout the analysis here we use the convention that a positive flux is upwards, that is, from the water surface to the overlying air.

Calculation of flux detection limits for the CO_2 flux measurements is described in Section S1. Determination of measurement time lag, and correction of high frequency signal attenuation in the closed-path IRGA measurements is described in Section S2.

For the duration that the open lead mast was in operation, the necessary input measurements were available to allow 1206 30-min CO_2 flux measurements from the closed-path IRGA. Standard statistical tests for skewness, kurtosis (Vickers & Mahrt, 1997) and stationarity (Foken & Wichura, 1996) were applied to assess the suitability of the measurements for flux calculation. The statistical tests were failed by ~37% of the flux measurements and these were removed, leaving 754 fluxes for analysis.

Net radiative fluxes were determined for the lead water surface following Dickey et al. (1994) using the measured downwelling short and long-wave radiation measurements, lead surface temperature and albedo estimated following Payne (1972). Buoyancy flux (β, $m^2\ s^{-3}$) into the lead waters was determined from the net radiative fluxes and the turbulent heat fluxes following MacIntyre et al. (2009).

2.3.2. Atmospheric and Waterside pCO_2

The CO_2 dry mole fraction measurements from the closed-path IRGA were converted to pCO_2a using measurements of temperature, humidity and pressure made on the mast, and the measurements averaged to the 30-min flux measurement time. Waterside CO_2 was measured at a depth of 0.5 m in the open lead using the CO_2-Pro CV membrane equilibration instrument. The sensor was factory calibrated from 0 to 600 ppm CO_2 prior to deployment, with a manufacturer-specified accuracy of 0.5%. The instrument sampled the seawater directly using a Sea-Bird Scientific SBE 5P submersible pump and measures the mole fraction of CO_2 in moist air in equilibration with the sampled water. The mole fraction is converted to CO_2 partial pressure (pCO_2w) using the sensor's measurement of gas stream pressure. The water-air partial pressure difference is then calculated directly.

2.3.3. Lead Dimensions and Flux Footprint

Both the ice floe and the lead were dynamic. The combined system moved and rotated with the surrounding ice pack. For ease of reference, a local coordinate system, "loc" is defined, with the mast located at the origin and the open lead hut located 137 m N^{loc} of the mast. The open lead was generally located from NNE^{loc} clockwise around to SWW^{loc} of the mast. The open lead varied in shape and size significantly during the measurement period (Figure 2a), depending on the meteorological conditions and the movement of the surrounding ice pack. The spatial dimensions of the lead were determined using a hand-held laser range finder (Naturalife PF4). Measurements were taken of the distance to the near and far shores of the lead, from a position adjacent to the mast at radial intervals of ~22.5°. Lead dimension measurements were attempted twice daily during the period of mast operation. Measurement was not always possible, for example, when precipitating particles prevented an accurate laser reading. Error in determining the lead dimensions results primarily from interpolation of the ice edge between the measurements, error in the positioning of the laser relative to the mast, and error in determining the edge of the lead. Measurement error due to the positioning of the ranger is estimated as ± 0.5 m. The laser signal is poorly reflected by water, which can lead to a possible bias in the determined dimensions. Measurement error in determining the edge of the lead is estimated as underestimation of up to 10% in near shore distances, and overestimation of up to 10% in far shore distances. The distance of the lead far shores varied from ~50 to > 450 m, and was generally greatest in the SW^{loc} and S^{loc} directions.

Fetch for each flux measurement was determined from the distance between the near and far shores in the mean wind direction. The spatial dimensions of the surface area contributing to the flux, and the relative contribution of locations within that area, are estimated by flux footprint models. There are numerous footprint models of varying complexity and typically with validation for different, specific atmospheric conditions (see Vesala et al., 2008 for a review of footprint models and their limitations). Here we estimate

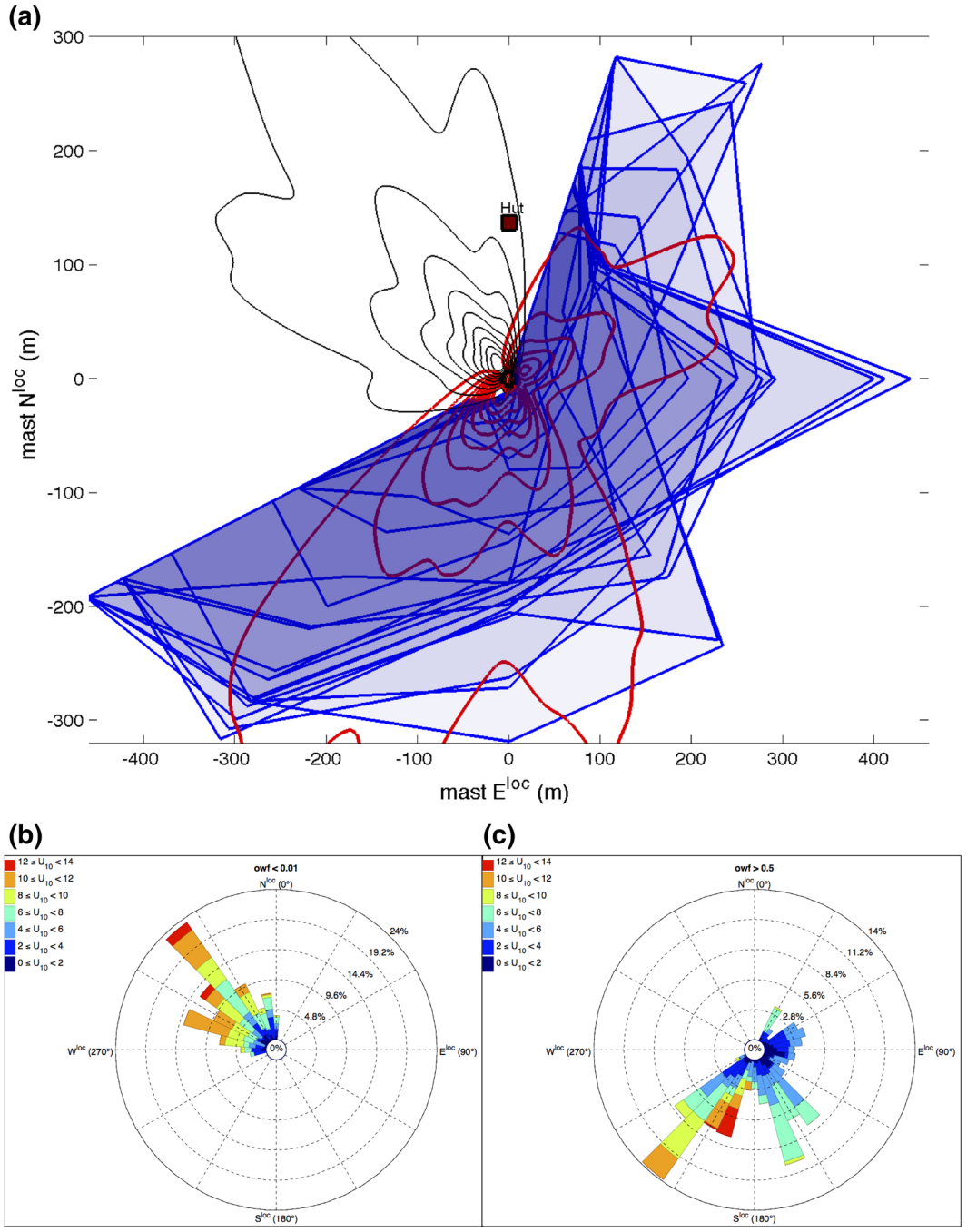

Figure 2. (a) Open lead dimensions and K15 flux footprint climatology estimates shown in mast-relative coordinates, with the mast located at 0 N^{loc}, 0 E^{loc}. The lead edges (blue lines) were determined on a near-daily frequency. Shading indicates the relative proportion of experiment time that a location was open water. Contours indicate footprint climatology flux contributions for the duration of the experiment in steps of 10% from 10% to 90%, for $owf > 0.5$ (red) and $owf < 0.01$ (black). Lower plots are windroses of 30-min average 10-m wind speeds and directions for (b) measurements with $owf < 0.01$ and (c) measurements with $owf > 0.5$. Directions are in the local frame of reference, direction widths are 10°, color indicates wind speed range and radius shows the fractional contribution to the set of winds shown.

the footprint using a two-dimensional model (Kljun et al., 2015, hereafter K15). In contrast to other commonly used analytical and parametric models, K15 has been validated through comparison with a Lagrangian particle dispersion model (itself tested using, e.g., wind tunnel and tracer release experiments) and is shown to be appropriate for a wide range of surface and atmospheric conditions and turbulence regimes. Validation of footprint models is a challenging task, and as far as we are aware no such testing for any model has been carried out in a sea ice environment. Results from the K15 model are compared with other estimates of the footprint and the resulting uncertainty discussed in Section 4.1.

For each flux measurement, the footprint was rotated into the mean wind direction and the nearest-in-time lead dimensions were used to determine the relative proportions of the footprint over water and over ice (Figure 2a). An open water fraction, *owf*, is defined as the proportion of the flux footprint that occurs over the lead water surface.

The *owf* can be used to partition the measured CO_2 flux, $F_{c,\ m}$, into the contribution through the water surface $F_{c,\ ow}$, and that through the ice/snow surface $F_{c,\ \mathrm{ice}}$ (Loose et al., 2014; Prytherch et al., 2017):

$$F_{c,m} = \left(1 - owf\right)F_{c,\mathrm{ice}} + owf\ F_{c,ow} \tag{5}$$

At the open lead site, melt ponds were only present during the first week of measurements, when the flux footprint was almost entirely over the lead (Section 3.1). As such, we omit an additional term from Equation 5 for fluxes through melt pond surfaces (Prytherch et al., 2017).

2.3.4. Gas Transfer Velocity

The gas transfer velocity through the water surface is determined from $F_{c,\ ow}$ using the normalized form of Equation 1:

$$k_{660,ow} = \left(F_{c,ow} \,/\, \left[K0\,\Delta p\mathrm{CO}_2\right]\right)\left(Sc \,/\, 660\right)^{1/2} \tag{6}$$

where $k_{660,\ ow}$ is the measured gas transfer velocity normalized to a Schmidt number (Sc) of 660 to account for the temperature dependence of seawater molecular diffusivity and viscosity (W14). The temperature used to determine Sc is the lead surface temperature determined by the KT15. IIp radiometer. The radiometer measurement is first corrected for sky reflection using an empirically derived correction (Hignett, 1998) and the downwelling short- and long-wave radiation measurements. The solubility, *K0*, is determined following Weiss (1974) from the lead's surface temperature, and from salinity as measured from *Oden's* pumped underway line that draws from a depth of 8 m. There were 628 k_{660} measurements with all necessary inputs derived from flux measurements that passed the statistical tests.

If $F_{c,\ \mathrm{ice}}$ is known or can be estimated, then $F_{c,\ \mathrm{ow}}$ can be determined from the measured CO_2 flux using Equation 5. For the analysis here, a minimum *owf* criteria of 0.5 was set, resulting in 383 $F_{c,\ ow}$ measurements and 359 $k_{660,\ ow}$ measurements available for analysis. A higher criteria reduces the number of measurements available for analysis, whilst a lower criteria decreases the sensitivity of the measurement (Section S1), demonstrated with the correlation of quadratic least squares regressions of $k_{660,\ ow}$ to U_{10}. Scaling the fluxes by *owf* also requires that the flux detection limit be scaled. An *owf* limit of 0.5 doubles the flux uncertainty for a given $\Delta p\mathrm{CO}_2$ and U_{I0}, all else being equal (Figure S1). For the closed-path IRGA sensitivity determined empirically here, a U_{10} of 8 m s^{-1}, $|\Delta p\mathrm{CO}_2|$ of 86 μatm (≈88 ppm) and *owf* of 0.5 gives an individual flux uncertainty of ~25%. For a wind speed of 2 m s^{-1}, the individual flux uncertainty is approximately 66%. For the open-path, the corresponding individual flux uncertainties are 105% and 266%. Fluxes are defined as over ice/snow surfaces ($F_{c,\ \mathrm{ice}}$) if $owf < 0.01$, a criteria met by 280 F_c measurements. For fluxes with *owf* between 0.5 and 0.01 (91 F_c measurements, 12% of the total) the measured flux may contain significant contributions from both water and ice surfaces. As such, we do not analyze these measurements further.

2.4. Density Perturbations and Water Vapor Cross-Sensitivity

A well-known issue for EC measurements of mass fluxes determined from density measurements is that they must be corrected for density perturbations caused by pressure, temperature and water vapor (Webb et al., 1980). Uncertainty in the measurements required for the correction, particularly of water vapor, can cause significant flux biases. The closed-path IRGA measures H_2O and CO_2 density, and determines dry mole fractions from these in real-time using measurements of temperature, pressure and humidity made inside the infrared measurement cell. Temperature equilibration in the sample inlet reduces the magnitude of the correction for temperature fluctuations for the closed path measurements. The colocation of the temperature pressure and humidity measurements in the IRGA measurement cell enables the density correction for the closed-path IRGA to be more precise than for the open path, and partly explains the greater sensitivity of this system (Section S1).

Measurement of CO_2 by absorption-based sensors such as IRGAs is directly affected by spectral cross-talk from the H_2O signal (e.g., Blomquist et al., 2014). This spectral interference results in a cross-sensitivity to water vapor in the CO_2 signal. This cross-talk has presented a significant obstacle to CO_2 flux measurement, particularly in environments such as the open ocean with relatively large H_2O fluxes and small CO_2 fluxes (Landwehr et al., 2014; S. D. Miller et al., 2010; Prytherch et al., 2010). A now widely-accepted approach is to dry the airstream prior to measurement, for example, with an inline Nafion membrane moisture exchanger (Blomquist et al., 2014; S. D. Miller et al., 2010).

The moisture-flux dependent error in F_c was characterized by Blomquist et al. (2014) as a cross-talk error proportionality coefficient, μ. From field and laboratory experiments, Blomquist et al. determined that for a closed-path LI-COR 7200 IRGA, $\mu = 0.1$ ppm kg g^{-1}. For their field measurements in the equatorial Indian Ocean (mean latent heat flux, $F_l = 100$ W m^{-2}, equivalent to a specific humidity flux of ~0.0343 g kg^{-1} ms^{-1}; small CO_2 flux resulting from small ΔpCO_2 and light winds), the humidity cross talk error in F_c from an undried-airstream closed-path IRGA was more than 7 times the magnitude of the flux measured with a dried-airstream closed-path IRGA. Both F_l and F_c were positive (upwards) and correcting for the cross-talk error acts to reduce the measured F_c. When conditions are more suited to CO_2 flux measurement, airstream drying may not be required. For example, closed-path IRGAs sampling from either dried or non-dried airstreams were shown to measure similar F_c when F_l was less than 7 W m^{-2} (Honkanen et al., 2018; Landwehr et al., 2014).

For the measurements reported here, it was not possible to deploy a drying system due in part to power (and hence pump) limitations at the measurement site. Measurement of F_c without airstream drying was possible because the humidity flux was very small and ΔpCO_2 relatively large. The mean absolute F_l measured with the open-path IRGA was 4.5 W m^{-2} (≈0.0014 g kg^{-1} m s^{-1}). The F_l measured by the closed-path was lower, 0.6 W m^{-2} (≈1.8 10^{-4} g kg^{-1} m s^{-1}) (Figure 3h). The closed path humidity flux measurement is not corrected for high frequency spectral attenuation, which is observed to be much higher (>1 order of magnitude) than the equivalent signal loss for CO_2 (e.g., Butterworth & Miller, 2016b; Yang et al., 2016). Here, the open-path IRGA is preferred for the determination of F_l, but the cross-talk error in F_c measured by the closed-path IRGA is dependent on F_l as measured in that system. For the lead water flux measurements, the low humidity flux, combined with a large CO_2 signal driven by the persistent large ΔpCO_2 in the open lead (mean ≈ −85 μatm; Section 3.1) resulted in an average humidity cross-talk correction in the closed-path IRGA F_c of ~1%. The direction of F_c was downwards, opposite to F_l, and hence the humidity cross-talk correction acts to increase the measured F_c. It was not possible to apply the frequency-dependent cross-correlation approach to correcting water vapor cross-sensitivity (Blomquist et al., 2014; Edson et al., 2011) due to the small heat fluxes and the lack of another independent scalar flux measurement.

3. Results

3.1. Meteorology

For the first 14 days of measurements (August 17–10:00 August 31), the wind measured at the mast was mostly flowing over the lead waters. Following this open water period, the wind measured at the mast was mostly flowing over ice until the end of measurements at 20:00 September 12. Wind speeds at the open

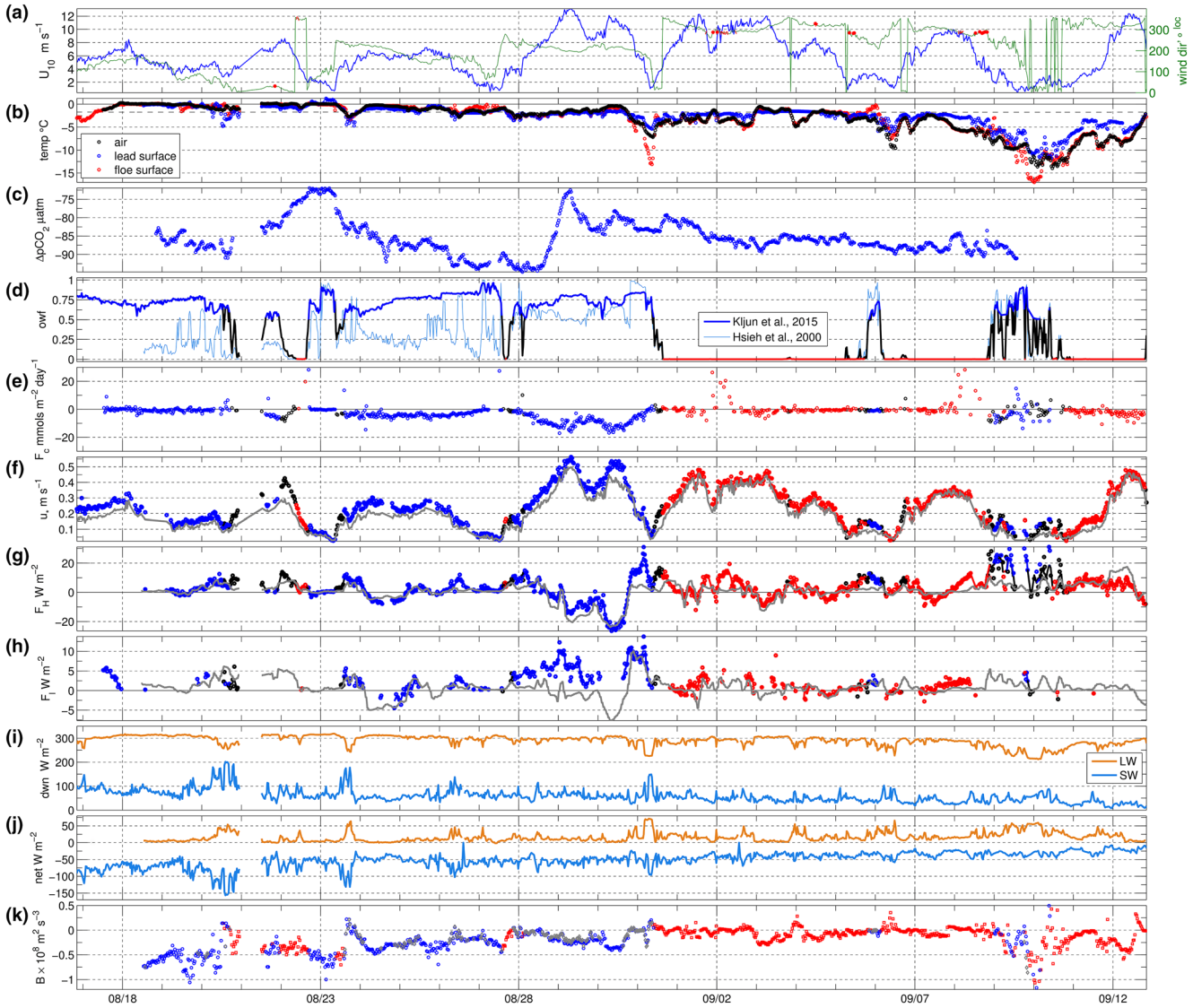

Figure 3. Time series from the open lead site for the period of closed-path IRGA F_c measurement. All measurements are 30-min averages or fluxes. (a) Wind speed and direction in mast reference frame. Wind directions when *Oden* was upwind of the mast (±5°) are indicated by red points. (b) Temperature of air (black), the lead surface determined by KT15 IR sensor (blue) and ice surface determined by KT15 IR sensor mounted on *Oden* (red). The dashed line is the freezing point of surface seawater. (c) Water–air pCO_2 difference. (d) Open water flux footprint fraction *owf* determined using K15, H00 and the equal weight method. For the K15 model, blue indicates *owf* > 0.5, red indicates *owf* < 0.01. (e) Flux of CO_2, $F_{c,m}$, measured by closed-path IRGA. (f) Friction velocity. (g) Sensible heat flux. (h) Latent heat flux determined by the open-path IRGA. (i) Downwelling long- and short-wave radiation. (j) Lead surface net long- and short-wave radiation flux. (k) Lead surface buoyancy flux using turbulent heat flux estimates of Smith (1988). Buoyancy flux determined with measured turbulent heat fluxes shown as gray diamonds. Upwards fluxes are positive. For e through h and k, color indicates *owf* as in (d) In (f–h), the gray lines are the model estimates of Smith (1988).

lead site were generally moderate (30-min average U_{10} 6.0 m s^{-1}) with several periods of higher winds, and a maximum 30-min U_{10} of 13.1 m s^{-1} (Figure 3a). Higher winds were generally from NW^{loc} and SW^{loc} directions (Figure 2b). For the open water period, the highest winds were from the S^{loc} and SW^{loc} with some moderate winds from SSE^{loc} (Figure 2c).

Air and surface temperature were typically 0 to −2°C during the open water period, typical for the sea-ice melt season. After this date, temperatures dropped to around −4°C before rising again to near freezing on September 3, then decreasing sharply around September 6. Surface freezing is determined by the complete surface energy balance. For the observations here, the surface energy balance followed the surface

temperatures and the onset of the autumn freeze up (determined following Tjernström et al., 2012) was estimated as August 28. Conditions remained variable following the onset of freeze up and the passage of storm systems led to higher winds and marked increases in temperatures.

For the open water period the surface temperature of the lead waters varied between 0°C and the freezing point of ∼−1.7°C (Figure 3b). Prior to August 31 there are occasional periods with lead temperatures lower than the freezing point, likely associated either with initial ice formation or drifting sea ice entering the infrared radiometers target area. The pCO_2w sensor was removed September 9 14:00 due to increasing ice build-up, and the majority of the lead became frozen over around September 10.

During the measurement period examined here pCO_2a was 394.1 ± 2.6 μatm (uncertainties are given as ± *s.d*, the sample standard deviation, unless otherwise stated), and pCO_2w 307.9 ± 4.6 μatm. The mean ΔpCO_2 was −85.4 ± 4.7 μatm. Throughout the measurement period the ΔpCO_2 shows a general slow decrease from decreasing pCO_2w (Figure 3c), presumably due to primary production within the lead. This slow decrease is marked by two periods (around August 22 and August 29) of sharp increase in pCO_2w following periods of higher winds and the resulting increase in mixing, gas transfer and the resulting increased equilibration of the lead waters with the atmospheric CO_2.

Sea-ice drift velocity at the mast site during the measurement period, determined from GPS measurement, was 0.12 ± 0.08 m s^{-1}, and the mean ratio of ice drift velocity to U_{10} was 0.018 ± 0.006. Sea-ice surfaces in the vicinity of the mast were generally covered with snow. Snow depth surveys over the ice floe on September 7 and September 14 determined median snow depths of 8.6 ± 7.4 cm and 10.6 ± 4.2 cm respectively. Cumulative snow depth measurements from an automated snow buoy deployed in the center of the ice floe on August 27 determined ∼2 cm snow accumulating between buoy deployment and the end of the ice camp in mid-September. Melt ponds were present on the ice floe at the beginning of the lead measurement period, though there were none in the immediate vicinity (within 50 m) of the mast. For this period the majority of the flux footprint was over water. From around August 24 to the end of measurements, a period which includes nearly all the over-ice flux measurements, melt ponds surfaces were frozen and increasingly snow covered.

3.2. Heat and Momentum Flux

Compared to CO_2 flux, the relative difference in flux magnitude due to surface type (ice or water) for heat and momentum fluxes is expected to be small. As such, we do not apply a form of Equation 5 to partition the heat and momentum fluxes. Friction velocity measurements (Figure 3f) are slightly higher than a bulk relationship (Smith, 1988), and the difference is greater for measurements determined with $owf > 0.5$. This may be due to increased drag from the lead edges. Normalized momentum flux cospectra (shown for $U_{10} > 4$ m s^{-1}) have a similar form for measurements over both ice and water surfaces (Figure 4), and agree with the theoretical form determined for measurements over uniform terrestrial surfaces with neutral stability (Kaimal et al., 1972). Ogive forms of the cospectra asymptote to 0 and 1 at low and high frequencies respectively, indicating that the full range of turbulent frequencies is measured.

EC sensible heat fluxes are small, typically less than 20 W m^{-2} (Figure 3g). Sonic temperature cospectra agree broadly with the theoretical neutral Kaimal form for measurements over water and ice. EC latent heat flux determined with the open-path IRGA is also small, generally <5 W m^{-2} with the exception of the period August 29–August 31, when fluxes are up to ∼10 W m^{-2} (Figure 3h). Despite the small flux magnitude, over water the latent heat flux cospectra (Figure 4) approximate the theoretical neutral Kaimal form, except at low frequencies, where the averaged cospectra are approximately zero below a normalized wave number of 0.002. Over ice, the latent heat fluxes have substantial noise at the lower frequencies. A more detailed analysis of the heat and momentum fluxes will be the subject of a subsequent manuscript.

3.3. Buoyancy Flux

Clear sky conditions, resulting in reduced longwave and increased shortwave downwelling radiation (Figure 3i) typically coincided with weaker winds. The net longwave radiation (Figure 3j, positive for upwards

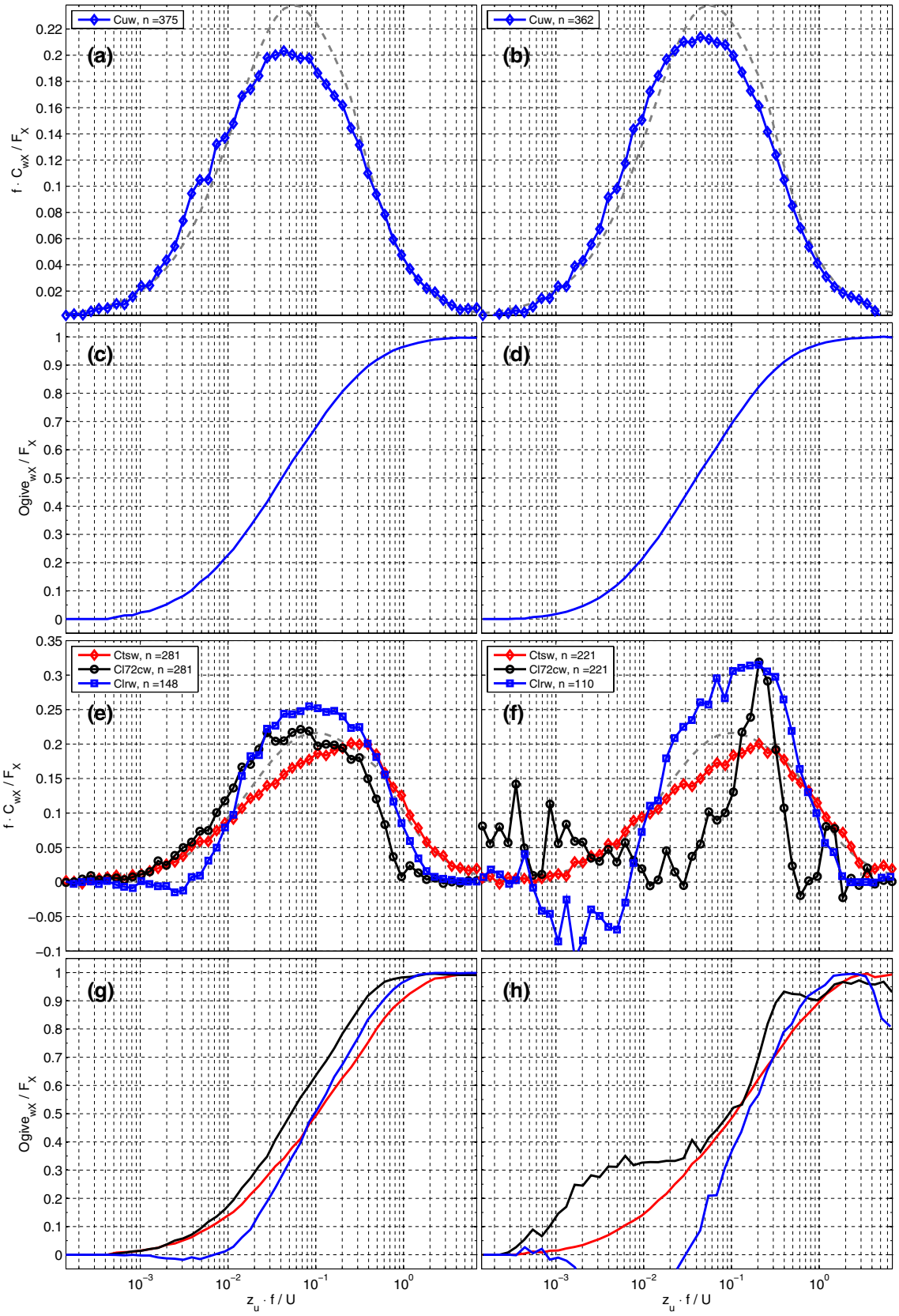
Cuw, n =375
(a)
Cuw, n =362
(b)
(c)
(d)
Ctsw, n =281
Cl72cw, n =281
Clrw, n =148
(e)
Ctsw, n =221
Cl72cw, n =221
Clrw, n =110
(f)
(g)
(h)
f · C_wX / F_X
Ogive_wX / F_X
z_u · f / U

flux) was positive during these periods, and at times large enough to result in a positive β (Figure 3k, cooling of the lead surface waters). These periods, indicating convective conditions in the upper lead waters, occurred sporadically prior to the freeze up, and then occurred often.

In the results, β was determined using the bulk model estimates of the turbulent heat flux (Smith, 1988) to increase data availability. The estimates of β determined from the directly measured heat fluxes (Figure 3k gray diamonds) agreed closely with those determined from the bulk model.

3.4. Ice/Snow–Atmosphere CO_2 Flux

For the periods when $F_{c,\,ice}$ was determined (*owf* < 0.01; Figure 3e) winds were almost entirely from the NW^{loc} (Figures 2b and 3a). In general, the measured $F_{c,\,ice}$ are relatively small (median −4.3 ± 4.2 mmols m^{-2} day^{-1}). For low wind periods with U_{10} < 5 m s^{-1}, the median flux was −1.3 mmol m^{-2} day^{-1}. The variability in the individual measurements (*s.d* for these periods was 1.9 mmol m^{-2} day^{-1}) results in some upwards fluxes, with a maximum upwards flux of +2.2 mmol m^{-2} day^{-1}. For the periods September 1 12:00–September 2 12:00 and September 7 18:00–September 9 00:00, the over-ice F_c are larger and much more variable (median 5.9 ± 21.2 mmols m^{-2} day^{-1}) with the maximum magnitude F_c +62.6 mmols m^{-2} day^{-1} (not shown). The sensible heat flux measurements (Figure 3g) are also higher than the bulk estimate for these two periods. There were relatively high off-ice winds during these two periods (mean 30-min U_{10} 8.7 ± 2.2 m s^{-1}). The high ice/snow-surface fluxes may result from release of CO_2 stored in snow through wind-driven pressure pumping (e.g., Bowling & Massman, 2011; Takagi et al., 2005), processes poorly understood in snow over sea ice. While *Oden* was upwind of the open lead mast during the high flux periods (Figure 3a), contamination of the measurements from *Oden's* emissions was not apparent in the pCO_2a measurements.

With the two anomalous periods excluded, the $F_{c,\,ice}$ measurements were less variable with a small median downward flux (−0.7 ± 1.3 mmols m^{-2} day^{-1}) and a maximum magnitude of −6.5 mmols m^{-2} day^{-1}. The winds for these fluxes were slightly lower (U_{10} 7.5 ± 2.8 m s^{-1}). These flux values are of similar magnitude to those observed for snow-covered sea ice during winter, spring, and early summer using chamber-based measurements (Delille et al., 2014; Geilfus et al., 2012, 2015; Nomura et al., 2010, 2013, 2018) and closed-path eddy covariance (Butterworth & Else, 2018; Sievers et al., 2015). These are the first reported measurements of sea-ice-atmosphere CO_2 flux obtained in the late summer and fall freeze up periods that we are aware of.

The $F_{c,\,ice}$ measurements exhibit a weak relationship with ice surface temperature (as determined for the snow and ice surface adjacent to *Oden's* mooring). The relationship, with larger downwards fluxes at higher temperatures and fluxes close to zero when temperatures fall to −5°C or less, is similar to one observed for CO_2 flux over Antarctic sea ice (Delille et al., 2014) but highly scattered with poor correlation (Figure 5a; linear least squares fit $r = -0.19$). The poor correlation in these measurements may result from the spatial separation between the flux and ice temperature measurements. The fluxes at warmer temperatures are smaller than those observed by Delille et al. (2014), possibly due to different snow coverage, though these observations were not available within the flux footprint. The ice fluxes have a stronger wind-speed dependence (Figure 5b; linear least squares fit $r = -0.44$), which may indicate high wind speed ventilation of the snow cover (Takagi et al., 2005). The wind speed dependence of the lead fluxes is stronger (Figure 5d; linear least squares fit $r = -0.9$).

Figure 4. Normalized, frequency weighted cospectra and ogives for flux measurements from the lead mast at U_{10} > 4 m s^{-1}. (a) Momentum flux cospectra for *owf* > 0.5. (b) Momentum flux cospectra for *owf* < 0.01. (c) Ogive for the data shown in (a) (d) Ogive for the data shown in (b) (e) Scalar flux cospectra of sonic temperature (red), latent heat (blue) and CO_2 (black) for *owf* > 0.5. (f) As for e for *owf* < 0.01. (g) Ogive for the data shown in (e) (h) Ogive for the data shown in (f) All cospectra are normalized by flux and frequency prior to averaging. Ogives are normalized by flux prior to averaging. Frequency in all panels is represented as a dimensionless wavenumber, $z_u f/U$, where f is measurement frequency.

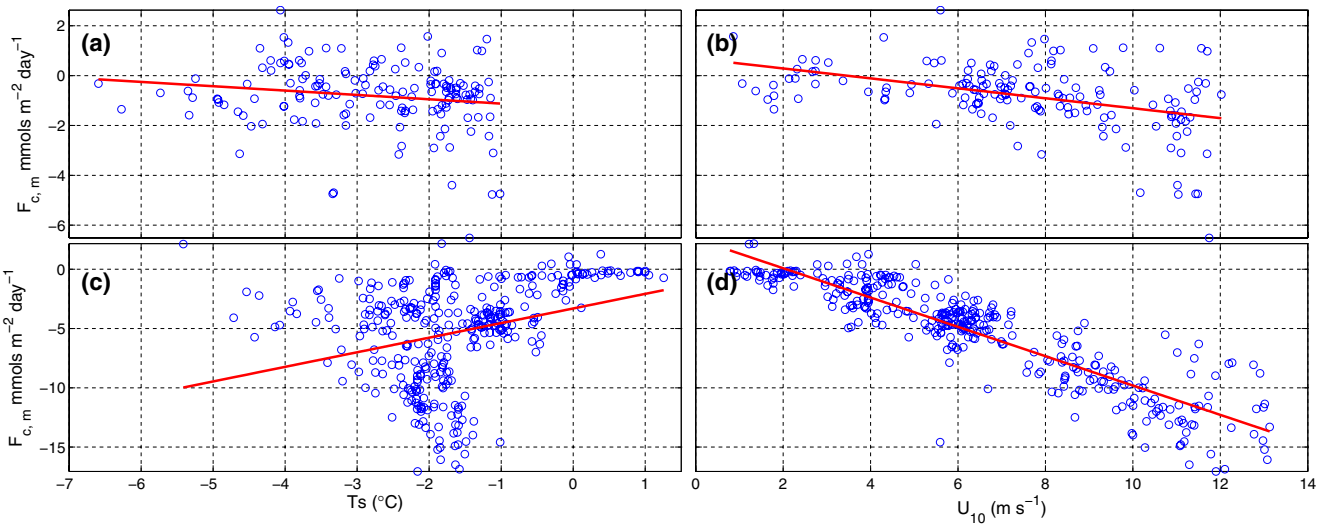

Figure 5. Relationship of $F_{c,\,m}$ to (a), (c) *Ts* and (b), (d) U_{10}. For (a) and (c) the fluxes are air-ice ($owf < 0.01$) and for (b) and (d) the fluxes are air-water ($owf > 0.5$). Ice flux measurements exclude the high flux periods between September 1 12:00 and September 2 12:00, and between September 7 18:00 and September 9 00:00. A linear least squares regression is shown for each data set (a, $r = 0.19$. b, $r = 0.44$. c, $r = 0.31$. d, $r = 0.90$).

3.5. Water-Atmosphere CO_2 Flux

$F_{c,\,ow}$ can be determined from Equation 5 if $F_{c,\,\mathrm{ice}}$ is known. We estimate $F_{c,\,\mathrm{ice}}$ for periods when $owf > 0.5$ using the median value of $F_{c,\,\mathrm{ice}}$ measured when $owf < 0.01$ (-0.7 mmols m^{-2} day^{-1}). Two anomalously high flux periods are excluded from the determination of this median (Section 3.4). For $F_{c,\,ow}$ with $owf > 0.5$, the flux direction was almost always downwards in the direction driven by the ΔpCO_2 gradient. The over-water CO_2 fluxes showed a strong relationship with wind speed. The wind-speed dependence is particularly noticeable in the period August 28–31, with 30-min average U_{10} up to 13.1 m s^{-1} (mean 9.4 ± 2.2 m s^{-1}) and a maximum F_c into the water of 22.4 mmols m^{-2} day^{-1} (median -12.4 ± 4.5 mmols m^{-2} day^{-1}).

For $F_{c,\,ow}$ with $owf > 0.5$, the majority of the measurements were obtained from NE$^{\mathrm{loc}}$, SSE$^{\mathrm{loc}}$, and SW$^{\mathrm{loc}}$ wind directions, and the fluxes measured at higher winds ($U_{10} > 8$ m s^{-1}) were entirely from the SW$^{\mathrm{loc}}$ direction (Figure 2c). The open lead was sometimes very large in this direction, with a fetch greater than 300 m (Figure 2a). The climatology of $owf > 0.5$ flux footprints shows that for fluxes from the SW$^{\mathrm{loc}}$ direction, the footprint region that lies over an ice surface is mostly the near region between the mast and the lead to the immediate SW$^{\mathrm{loc}}$ of the mast. Cospectra of $F_{c,\,ow}$ have the expected form, allowing for the high frequency tube attenuation effect (Section S2), and are similar to the other scalar fluxes (Figure 4). The $F_{c,\,\mathrm{ice}}$ cospectra are much noisier, with greater than expected low frequency signal, resulting from the much smaller signal in these measurements. The majority of the signal remains at the expected frequencies, peaking at a normalized wavenumber of 0.3.

3.6. Gas Transfer Velocity

Gas transfer measurements binned by wind speed (1 m s^{-1} width bins), have an approximately quadratic dependence on wind speed (Figure 6). A quadratic fit is determined from least squares regression:

$$k_{660} = 0.179\,U_{10}^2 \left(r^2 = 0.72\right) \tag{7}$$

The gas transfer relationship to wind speed determined here is slightly weaker than that in commonly used models of gas transfer derived for open ocean measurements: The ratio of the relationship, for winds above 2 m s^{-1}, to that of W14 is 0.71; for the dual tracer-derived relationship of Nightingale et al. (2000), the ratio is 0.69, and for the EC-derived cubic wind speed-dependent relationship of McGillis et al. (2001), the ratio is 0.59. For wind speeds above 5 m s^{-1}, Equation 7 is substantially higher (ratio of 1.32) than a relationship

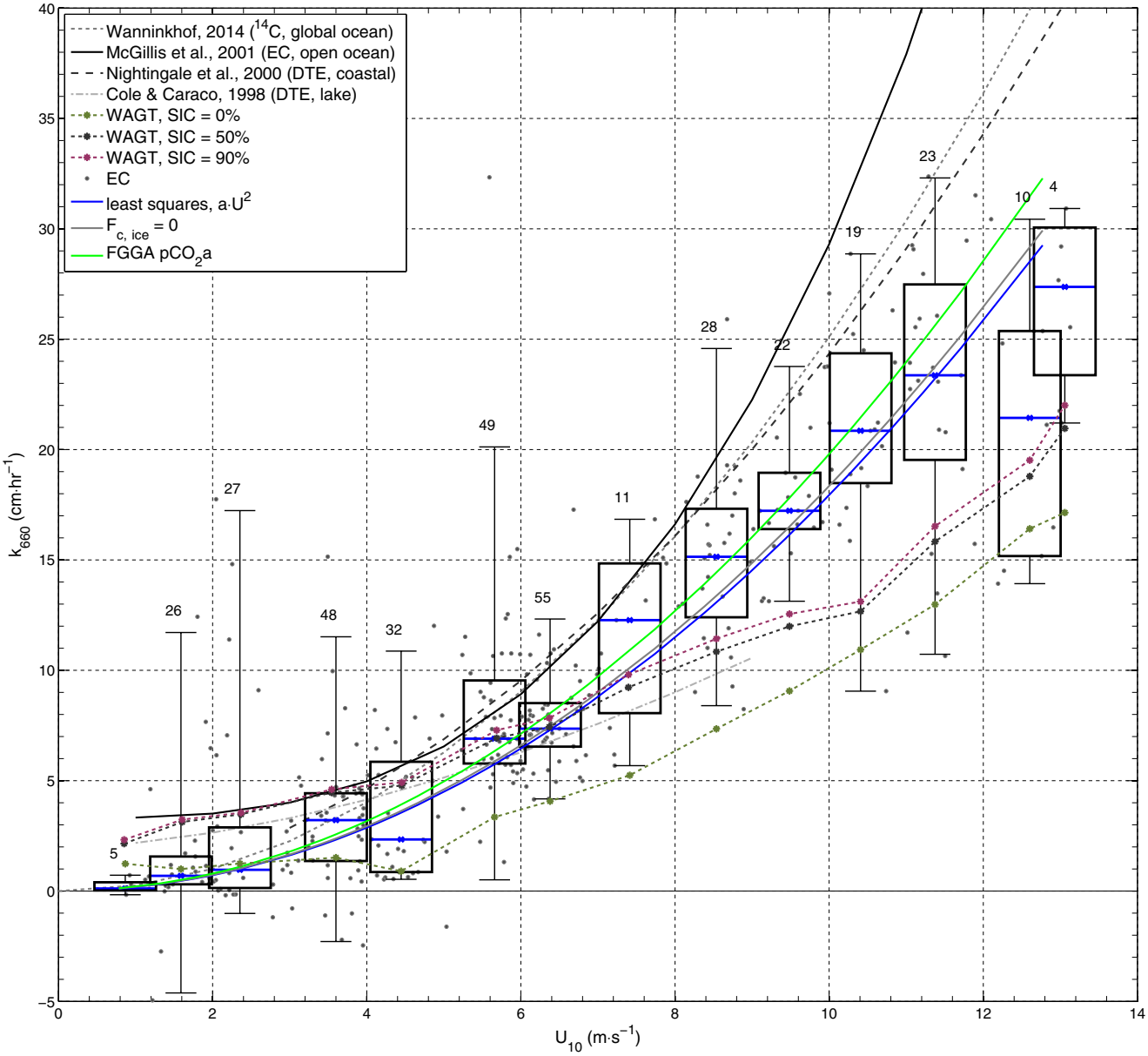

Figure 6. Observed relationship of k_{660} to U_{10} at the lead site. Gas transfer measurements shown as gray dots and binned in 1 m s^{-1} wide wind speed bins as box and whisker plots (percentiles 2.5, 25, 50, 75, 97.5). The number of measurements in each bin is indicated. Black and gray lines show published wind speed parameterizations of k_{660} as listed in the legend with the measurement type (radiocarbon inventory, 14C; EC or dual-tracer experiment, DTE), and location used to derive the parameterization. WAGT model predictions are shown for SIC of 0%, 50% and 90% (dotted lines and stars). Least squares quadratic fits are shown for the EC data (blue solid line); data with $F_{c,\ ice} = 0$ (gray line) and data with pCO_2a from the *Oden* foremast FGGA sensor (green line).

determined from dual tracer measurements frequently used to model gas transfer in lakes (Cole & Caraco, 1998). At lower wind speeds, Equation 7 is lower than this relationship. Note that the dual tracer measurements used to derive this model were only made during low to moderate wind speed conditions and are extrapolated here for winds over 9 m s^{-1}. The measurements were also compared with a parametric model of gas exchange in sea ice regions (WAGT: Bigdeli et al., 2018; Loose et al., 2014). The WAGT model predicts the effective gas transfer velocity for a given sea-ice concentration (SIC), k_{eff}, from inputs of wind and ice velocity, water and air temperature and SIC. Here, SIC of 0%, 50% and 90% are used to give a representative range and k_{660} is determined as $k_{660} = k_{eff}/(1\text{-SIC}/100)$. Compared with the measurements, the WAGT model over predicts for winds <6 m s^{-1} and under predicts at higher wind speeds.

4. Discussion

The directly determined gas transfer rates reported here have a reduced wind speed dependence relative to previously reported ship-based direct measurements from sea ice regions (Butterworth & Miller, 2016; Prytherch et al., 2017), which when scaled by *owf* have similar wind speed dependence to W14. The reduced wind speed dependence determined here is however, within the uncertainty range of the ship-based measurements. Measurements of wind and air-sea exchange from platforms such as ships and buoys are biased by flow-distortion-induced errors (Yelland et al., 2002) which can be exacerbated by platform motion (Prytherch et al., 2015). The ice floe in the vicinity of the mast was relatively flat, with only low ridges and snow drift (<20 cm height), and such biases are not expected to affect the measurements reported here. A relatively low measuring height in a fixed location also aids the determination of the flux footprint. For measurement at typical ship-mast heights with correspondingly larger footprints (>1 km scale), the *owf* must be determined from either processing of in situ imagery (Butterworth & Miller, 2016) or from satellite remote sensing of ice fraction (Prytherch et al., 2017). In situ imagery typically only sees the ice within a short distance (~200 m) of the ship, whilst satellite products average over an area typically much larger (>6 km^2) than a flux footprint. The resulting greater uncertainty in the ship-based measurements may explain the differences between them and the measurements reported here.

Despite the greater precision of measurements from a fixed mast, determination of gas transfer rates remains challenging, particularly in a sea-ice environment. There are many factors that can bias the measurements, for example, error in the determination of the flux footprint, error in determination of the lead dimensions, the presence of surfactants in the lead water, error in the determination of ΔpCO_2 and poor signal-to-noise ratio. These factors are examined in Section 4.1 below. Factors such as convection and waves that drive near surface turbulence and can influence gas exchange in addition to wind speed are discussed in Section 4.2.

4.1. Potential Sources of Bias

In K15, the authors compare their model with other available 2D footprint models. The parametric model of Hsieh et al. (2000, hereafter termed H00), extended to include crosswind area following Detto et al. (2006), is shown to give similar results to the analytical model of Kormann and Meixner (2001). We compare the footprint calculated using K15 with those calculated using H00. We find the H00 model to have a generally longer and wider footprint for the near-neutral stability conditions common in our measurements prior to the freeze up. Hence, *owf* determined from this model in near-neutral stability is often much lower than for that determined from K15 (Figure 3d). The H00 model includes a fixed stability limit (−0.04). For z_u/L, greater than this limit, where L is the Obukhov length, stability is termed neutral and the model parameters are set differently from the unstable periods. As such, when stability is close to this limit there can be rapid variations in footprint size and hence *owf*, as apparent around, for example, August 19 and August 25 (Figure 3d).

The impact on k of determining *owf* using the H00 model is shown in Figure 7a. Here, only periods where *owf* from each of the models was >0.5 were used. This removes the near-neutral periods that can cause rapid changes in the size of the H00 footprint and hence in *owf*. For this reduced dataset (145 measurements), the ratio of the quadratic fit with *owf* determined with K15, to W14, is 0.77. Determining *owf* using H00 gives a higher estimate of k (ratio of fit to W14 0.92) than from using K15. While it is not possible here to determine which of the available footprint models is more "correct", the K15 model is preferred due to its validation over a wider range of atmospheric conditions, and its lower sensitivity to small changes in atmospheric stability.

The determination of both *owf* and fetch is dependent on lead dimension measurements. The challenging measurement environment and manpower availability resulted in both low spatial resolution (~22.5°) and low measurement frequency (~daily), which will contribute to random error in the determination of the lead dimensions. In addition, there may be a bias resulting from the stronger laser return signal from ice edges and ridges, relative to water. This may result in a mean overestimation of the lead size, particularly for measurement of the distance to the far shore. This bias was estimated as up to 10% of each range meas-

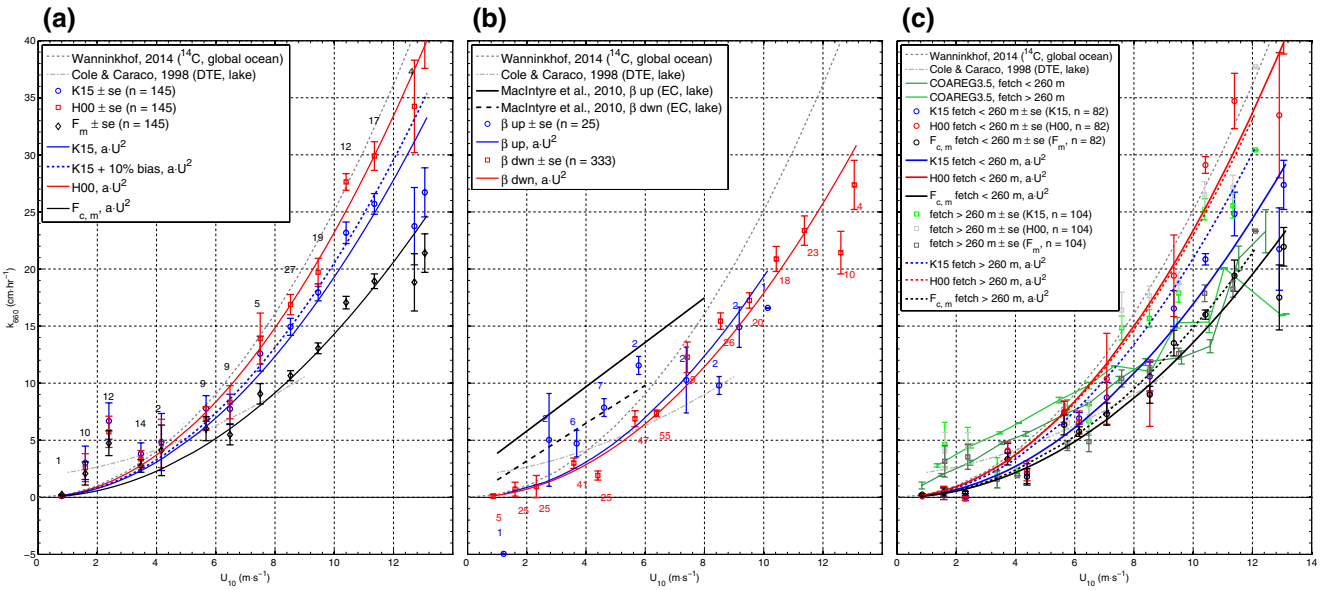

Figure 7. Observed dependence of k_{660} on U_{10} and: (a) choice of footprint model used to determine *owf*, with the models described in the text; (b) buoyancy flux into the lead water (β), with k_{660} measurements separated into β down (surface heating, red line) and β up (surface cooling, blue line) buoyancy groupings (c) fetch, with k_{660} separated into high (fetch > 260 m, red line) and low (fetch < 260 m, blue line) groupings for both the K15 (blue) and H00 (red) footprint models. The COAREG3.5 model estimates are shown separated into the same fetch groupings as for the measurements. For each panel, measurements are binned in 1 m s^{-1} wide wind speed bins with the number in each bin shown. The bin center shows the median of the binned measurements and the error bars show the standard error. Least squares quadratic fits are shown for each grouping. Gray lines show published wind speed parameterizations of k_{660} as listed in the legend with the measurement type and location.

urement. A set of *owf* and fetch measurements were determined assuming the maximum bias within this range (i.e., far-shore range measurements were reduced by 10%, and near-shore range measurements were increased by 10%) and the K15 footprint model, and the gas transfer velocities recalculated from Equations 5 and 6. Including this potential bias increased the observed quadratic wind speed dependence of the k measurements by ~5% (Figure 7a). The relationship remained suppressed relative to previous parameterizations, with the ratio of the quadratic fit to the relationship of W14 increased from 0.77 to 0.82.

Biologically-derived surfactants, in particular soluble surfactants, are widely found in ocean surface microlayers at wind speeds up to at least 13 m s^{-1} (Sabbaghzadeh et al., 2017) and act to reduce gas transfer through suppression of capillary-gravity waves (McKenna & McGillis, 2004). The ubiquitous nature of surfactants means that the data from which existing k parameterizations are derived is very likely influenced by the presence of surfactants. Surface microlayer samples were obtained from the lead waters during the course of the ice camp using a variety of different measurement methods. Preliminary analysis has determined surfactant enrichment factors similar to open ocean values close to the ice edge, with enrichment decreasing for samples further out from ice edge (pers. comm., T-B Robinson, U. Oldernburg). This suggests that the observed gas transfer suppression is not the result of high surfactant enrichment.

In the calculation of ΔpCO_2, pCO_2a was obtained from the closed-path IRGA on the open-lead mast. Atmospheric CO_2 partial pressure was also determined using a Los Gatos Research (LGR) Fast Greenhouse Gas Analyzer (FGGA) gas onboard *Oden*, sampling air from an intake on *Oden's* foremast at 20 m above the surface (Prytherch et al., 2017). The FGGA determines CO_2 dry mole fraction at 10 Hz from CO_2 absorption using internal cell pressure, temperature and water vapor measurements. Dry mole fractions were converted to pCO_2a using measurements of temperature, humidity and pressure made on the mast, and measurements averaged to the 30-min flux measurement time. While it is located >1 km horizontally away and ~18 m higher than the flux measurement location, this instrument has greater accuracy than the closed-path IRGA and may provide a more reliable measurement of mean atmospheric CO_2 concentration. The range of pCO_2a measured by the LGR was 381–394 μatm, and the pCO_2a was lower than that measured by the closed-path IRGA by 7.5 ± 1.5 μatm. If the FGGA pCO_2a measurements are used in place of those

from the IRGA to determine k, then the observed quadratic fit is higher, with a ratio of 0.79 relative to the relationship of W14 (Figure 6).

Instrument failures resulted in pCO_2w measurements only being made from one location in the lead waters, to the E^{loc} of the mast ~3 m from the ice floe edge. Horizontal gradients of pCO_2w within the lead waters are a potential source of error in the determination of k which may be dependent on relative wind direction and/or fetch. Large gradients would violate the stationarity assumption required for EC and may be removed by the flux quality control procedures. Vertical gradients in pCO_2w above the measurement depth (which would act to reduce ΔpCO_2 and so result in a low bias in the estimate of k) are expected to be small due to the persistent wind forcing and shallow measurement depth (0.5 m). The sustained higher winds from September 1 to 5 and on September 8 do not cause large increases in pCO_2w (Figure 3). For the location of the pCO_2w sensor, close to the mast, the winds here were largely off ice, and the waters around the sensor somewhat sheltered with minimal fetch. Hence the mixing and gas transfer in the vicinity of the sensor may have been smaller than in the lead away from the shore. Alternatively, the increased ice growth during these later periods may have suppressed the wind-induced mixing in the lead more generally, resulting in the smaller response of the measured pCO_2w to wind.

Measurement of the relatively small ice-atmosphere fluxes represents a signal to noise challenge. Following Blomquist et al. (2014), for the sensitivity determined for the closed path sensor (Section S1 and Figure S1), and assuming a gas transfer relationship (W14), we can estimate the minimum flux magnitude required for measurement with 100% error (i.e., the uncertainty in an individual flux measurement is the same magnitude as the true flux) as between 0.5 and 2.5 mmols m^2 day^{-1}, with higher flux magnitudes corresponding to higher winds. For the near ideal CO_2 measurement conditions reported here, the majority of the observed ice-atmosphere fluxes are within, or close to this somewhat arbitrary limit. An alternative approach is to set all $Fc_{,\,ice}$ to 0 in the determination of F_{ow} from Equation 5. This increases the wind speed dependence of k slightly (Figure 6), with the ratio of the quadratic fit to the relationship of W14 increased from 0.71 to 0.73. It is notable that the sensitivity determined here for the closed-path IRGA is approximately four times greater than that determined for the open-path IRGA (Figure S1). The inability of open-path sensors to determine small fluxes such as those measured over ice surfaces here may explain the disparity between early eddy covariance and chamber-based measurements of ice-atmosphere CO_2 flux.

4.2. Physical Influence

Convective conditions, indicated by surface cooling, resulted in higher k measurements for wind speeds between 2 and 6 m s^{-1} (mean convective to non-convective ratio 2.0, mean difference 3.6 cm hr^{-1}) (Figure 7b). The convective enhancement of k for these wind speeds is similar in absolute magnitude to that observed in a shallow lake, close to the Arctic circle in summertime (MacIntyre et al., 2010), though k is generally higher in the lake observations than in the lead.

There are only 25 flux measurements during surface cooling conditions (17 between 2 and 6 m s^{-1}), which occur infrequently during the summer melt season when the majority of the open lead flux measurements were made. Convective turbulence has only a minor role, relative to wind forcing, in summer polar air-sea exchange. Following the onset of the freeze up, convective conditions occur more frequently, and as leads and open water areas are still widespread during this period, convection may become a significant forcing.

Fetch observed during the experiment varied from 40 to 440 m. For winds above 7 m s^{-1} the fetch varied from 75 to 410 m. The gas transfer measurements are divided into high and low fetch groups, with the boundary (fetch = 260 m) chosen to ensure approximately equal numbers in each grouping at winds above 7 m s^{-1} (Figure 7c). For winds below 7 m s^{-1}, the standard error of the binned gas transfer velocity from the two fetch groups overlaps. For the higher winds, the greater fetch measurements have higher k. The lower fetch measurements have lower k by 17%. This fetch dependence is apparent in k calculated from *owf* determined using the K15 model, and also in k determined from $F_{c,\,m}$ using no *owf* scaling (Equation 5). For k calculated from *owf* determined using the H00 model, no fetch dependence is apparent (Figure 7c). Whereas the K15 footprint extent is typically less than the larger observed fetch, the extent of the H00 footprint is much larger, greater than the largest observed fetch. As such when using the H00 model increased

fetch results in higher *owf* and hence reduced $F_{c,\,ow}$, acting to remove the apparent fetch dependence in $F_{c,\,m}$. Note that the k measurements used are those for which *owf* from both footprint models is greater than 0.5. If only the K15 *owf* criteria is used (with 246 and 113 k measurements respectively for the low and high fetch groupings), the K15 k fits are visibly unchanged from those shown.

With short fetch and hence small wave heights, and with the surrounding ice pack suppressing swell, lead waters are more akin to deep, saline lakes than to open ocean waters. Gas transfer rates determined experimentally in lake environments (e.g., Cole & Caraco, 1998; MacIntyre et al., 2010; Wanninkhof, 1992) are lower than those observed in the open ocean. However, these measurements are obtained in limited wind speed ranges (below 9 m s^{-1} for the three experiments listed) and the determination of additional forcings has typically focused on factors (e.g., lake-bottom influence) not relevant to the central Arctic Ocean. At the higher winds measured during this experiment (above ~ 9 m s^{-1}), small breaking waves and whitecaps were observed in the lead. The influence of bubble-mediated exchange is not accounted for in parameterizations based on measurements at winds speeds below that required for wave breaking, or in any gas transfer parameterization based on dual-tracer measurement (e.g., Cole & Caraco, 1998; Nightingale et al., 2000). The observed fetch signal in k suggests fetch and wave-related forcing may have a role in air-sea gas transfer in sea ice regions, but the footprint model-dependence of this signal means further investigation is required. While the K15 model is preferred here as it has more extensive validation than other available 2D footprint models, it has not been tested in a sea-ice environment.

Fetch is determined implicitly from SIC in the sea-ice configuration of the WAGT model (Bigdeli et al., 2018). The fetch-limited configuration of the model, with SIC set to 0, has explicit fetch dependence. In both configurations, the model dependence on fetch and wind speed is weaker than for the observations reported here (Figure 6). The COAREG3.5 physical model (Blomquist et al., 2017) incorporates sea state dependent bubble-mediated gas transfer. The COARE model, with significant wave height determined from the fetch measurements using the relationship of Carter (1982), overestimates the observed gas transfer at wind speeds below ~7 m s^{-1} and underestimates at higher wind speeds (Figure 7c). The magnitude of the COARE model estimates of fetch dependence is approximately constant with wind speed, higher than relationship observed in the EC measurements at lower wind speeds and a weaker dependence than observed at the higher wind speeds. The COARE algorithm can be tuned to fit observations by modifying two constants that determine molecular sublayer resistance to gas transfer and the dependence on whitecap fraction of bubble-mediated transfer. Here we use values for the constants as determined during high wind conditions in the North Atlantic ($A = 1.2$, $B = 3.8$; Blomquist et al., 2017). Adjustments of these constants, as well as further development of the sea state dependence of the transfer coefficients within COARE, may lead to improved agreements between the model and observations reported here.

5. Conclusions

We report the first direct determination of gas transfer velocities in a sea-ice lead, from ice-based measurements at a lead in the central Arctic Ocean during the transition between summer melt and autumn freeze up seasons. The gas transfer velocities were determined from eddy covariance CO_2 flux measurements made during favorable conditions, that is, low humidity flux and high ΔpCO_2 conditions. Measurements were made of both lead water–atmosphere and ice/snow–atmosphere fluxes and are the first direct flux measurements reported for pack ice in the summer-autumn season. A flux footprint analysis was used to determine the flux into the lead surface from which the gas transfer velocity was derived.

Measurements were determined for wind speeds up to 13.1 m s^{-1}. The measured k_{660} has a quadratic wind speed dependence, ~ 30% lower than widely used open-ocean and coastal-ocean parameterisations (e.g., W14; Nightingale et al., 2000) and ~30% higher than a commonly used parameterization for gas transfer through lake surfaces (Cole & Caraco, 1998). The measurements exhibit a dependence on convection-driven turbulence, though the relatively few measurements with upwards buoyancy flux (cooling lead waters) suggest this is a minor driver of gas exchange for this location and season. Whilst the measurements also exhibit a fetch dependence, suggesting the importance of lead dimensions and the resulting wave characteristics on gas exchange, the apparent fetch dependence may also result from uncertainty in the flux footprint.

These results suggest that current methodology for estimating polar air-water carbon exchange, using open ocean gas transfer parameterizations either scaled linearly by open water fraction or enhanced above this scaling, over estimate gas exchange rates. While these observations demonstrate the requirements for parameterization of summer gas exchange, further observations are required, particularly for colder seasons when large heat fluxes from lead surfaces may drive strong convective turbulence. Improved estimates of gas transfer in sea-ice regions may require parameterizations that incorporate sea state dependency appropriate for lead scales and the deep, saline ocean conditions. Additional forcings of upper ocean turbulence, such as form drag from ice edges, may have greater impacts on leads of smaller scales than observed here.

Furthermore, scaling such parameterizations to regional gas exchange estimates will require incorporating lead width distributions, as observed with passive (Bröhan & Kaleschke, 2014) and active (Wernecke & Kaleschke, 2015) remote sensing, as well as wind speed and direction relative to lead orientation. Lead widths exhibit a power law distribution (Marcq & Weiss, 2012), hence a large fraction of total lead area will consist of leads smaller than that in this study. Direct determinations of gas exchange through such leads likely requires mobile observations with large footprint areas that can integrate varying lead scales (such as from planes and ships; Prytherch et al., 2017).

Data Availability Statement

All micrometeorological and gas exchange data from this project are available on The Bolin Center Database (https://bolin.su.se/data/ao2018-micromet-icefloe-5). Autonomous sea-ice measurements (snow depth) from August 16, 2018 to September 16, 2018 were obtained from http://www.meereisportal.de (grant: REKLIM-2013-04).

Acknowledgments
This work is part of the Arctic Ocean 2018 (AO2018) expedition and was funded by The Bolin Center for Climate Research. The Swedish Polar Research Secretariat (SPRS) provided access to the icebreaker *Oden* and logistical support. The authors are grateful to the Chief Scientists Caroline Leck and Patricia Matrai for planning and coordination of AO2018, and in particular to the SPRS logistical staff and *Oden*'s Captain Mattias Peterson and his crew for their invaluable support. We are also grateful to Prof. Michael Tjernström (Stockholm U., Sweden) and Prof. Ian Brooks (U. Leeds, UK) for providing instrumentation and invaluable advice.

References

Andreas, E. L., Horst, T. W., Grachev, A. A., Persson, P. O. G., Fairall, C. W., Guest, P. S., et al. (2010). Parameterizing turbulent exchange over summer sea ice and the marginal ice zone. *Quarterly Journal of the Royal Meteorological Society*, *136*(649), 927–943. https://doi.org/10.1002/qj.618

Bakker, D. C., Pfeil, B., Landa, C. S., Metzl, N., O'Brien, K. M., Olsen, A., et al. (2016). A multi-decade record of high quality fCO_2 data in version 3 of the Surface Ocean CO_2 Atlas (SOCAT). *Earth System Science Data*, *8*, 383–413. https://doi.org/10.5194/essd-8-383-2016

Bates, N. R., & Mathis, J. T. (2009). The Arctic Ocean marine carbon cycle: Evaluation of air-sea CO_2 exchanges, ocean acidification impacts and potential feedbacks. *Biogeosciences*, *6*(11), 2433–2459.

Bigdeli, A., Hara, T., Loose, B., & Nguyen, A. T. (2018). Wave attenuation and gas exchange velocity in marginal sea ice zone. *Journal of Geophysical Research: Oceans*, *123*, 2293–2304. https://doi.org/10.1002/2017JC013380

Blomquist, B. W., Brumer, S. E., Fairall, C. W., Huebert, B. J., Zappa, C. J., Brooks, I. M., et al. (2017). Wind speed and sea state dependencies of air-sea gas transfer: Results from the high wind speed gas exchange study (HiWinGS). *Journal of Geophysical Research: Oceans*, *122*(10), 8034–8062. https://doi.org/10.1002/2017jc013181

Blomquist, B. W., Huebert, B. J., Fairall, C. W., Bariteau, L., Edson, J. B., Hare, J. E., et al. (2014). Advances in air-sea CO_2 flux measurement by eddy correlation. *Boundary-Layer Meteorology*, *152*(3), 245–276. https://doi.org/10.1007/s10546-014-9926-2

Bowling, D. R., & Massman, W. J. (2011). Persistent wind-induced enhancement of diffusive CO_2 transport in a mountain forest snowpack. *Journal of Geophysical Research*, *116*, G04006. https://doi.org/10.1029/2011jg001722

Bröhan, D., & Kaleschke, L. (2014). A nine-year climatology of Arctic Sea ice lead orientation and frequency from AMSR-E. *Remote Sensing*, *6*(2), 1451–1475. https://doi.org/10.3390/rs6021451

Brumer, S. E., Zappa, C. J., Blomquist, B., Fairall, C. W., Cifuentes-Lorenzen, A., Edson, J. B., et al. (2017). Wave-related Reynolds number parameterizations of CO_2 and DMS transfer velocities. *Geophysical Research Letters*, *44*, 9865–9875. https://doi.org/10.1002/2017GL074979

Burba, G. G., McDermitt, D. K., Grelle, A., Anderson, D. J., & Xu, L. (2008). Addressing the influence of instrument surface heat exchange on the measurements of CO_2 flux from open-path gas analyzers. *Global Change Biology*, *14*(8), 1854–1876. https://doi.org/10.1111/j.1365-2486.2008.01606.x

Butterworth, B. J., & Miller, S. D. (2016). Air-sea exchange of carbon dioxide in the Southern Ocean and Antarctic marginal ice zone. *Geophysical Research Letters*, *43*, 7223–7723. https://doi.org/10.1002/2016GL069581

Butterworth, B. J., & Else, B. G. T. (2018). Dried, closed-path eddy covariance method for measuring carbon dioxide flux over sea ice. *Atmospheric Measurement Techniques*, *11*(11), 6075–6090. https://doi.org/10.5194/amt-11-6075-2018

Butterworth, B. J., & Miller, S. D. (2016). Automated underway eddy covariance system for air-sea momentum, heat, and CO_2 fluxes in the Southern Ocean. *Journal of Atmospheric and Oceanic Technology*, *33*(4), 635–652. https://doi.org/10.1175/JTECH-D-15-0156.1

Carter, D. J. T. (1982). Prediction of wave height and period for a constant wind velocity using the JONSWAP results. *Ocean Engineering*, *9*(1), 17–33. https://doi.org/10.1016/0029-8018(82)90042-7

Cole, J. J., & Caraco, N. F. (1998). Atmospheric exchange of carbon dioxide in a low-wind oligotrophic lake measured by the addition of SF_6. *Limnology & Oceanography*, *43*(4), 647–656. https://doi.org/10.4319/lo.1998.43.4.0647

Delille, B., Vancoppenolle, M., Geilfus, N. X., Tilbrook, B., Lannuzel, D., Schoemann, V., et al (2014). Southern Ocean CO2 sink: The contribution of the sea ice. *Journal of Geophysical Research: Oceans*, *119*, 6340–6355. https://doi.org/10.1002/2014JC009941

Detto, M., Montaldo, N., Albertson, J. D., Mancini, M., & Katul, G. (2006). Soil moisture and vegetation controls on evapotranspiration in a heterogeneous Mediterranean ecosystem on Sardinia, Italy. *Water Resources Research*, *42*, W08419. https://doi.org/10.1029/2005wr004693

Dickey, T. D., Manov, D. V., Weller, R. A., & Siegel, D. A. (1994). Determination of longwave heat flux at the air-sea interface using measurements from Buoy platforms. *Journal of Atmospheric and Oceanic Technology*, *11*(4), 1057–1078. https://doi.org/10.1175/1520-0426(1994)011<1057:dolhfa>2.0.co;2

Edson, J. B., Fairall, C. W., Bariteau, L., Zappa, C. J., Cifuentes-Lorenzen, A., McGillis, W. R., et al. (2011). Direct covariance measurement of CO_2 gas transfer velocity during the 2008 Southern Ocean Gas Exchange Experiment: Wind speed dependency. *Journal of Geophysical Research*, *116*. https://doi.org/10.1029/2011jc007022

Else, B. G. T., Papakyriakou, T. N., Galley, R. J., Drennan, W. M., Miller, L. A., & Thomas, H. (2011). Wintertime CO2 fluxes in an Arctic polynya using eddy covariance: Evidence for enhanced air-sea gas transfer during ice formation. *Journal of Geophysical Research*, *116*, C00G03. https://doi.org/10.1029/2010JC006760

Fanning, K. A., & Torres, L. M. (1991). 222Rn and 226Ra: Indicators of sea-ice effects on air-sea gas exchange. *Polar Research*, *10*(1), 51–58.

Foken, T., & Wichura, B. (1996). Tools for quality assessment of surface-based flux measurements. *Agricultural and Forest Meteorology*, *78*(1), 83–105. https://doi.org/10.1016/0168-1923(95)02248-1

Geilfus, N. X., Carnat, G., Papakyriakou, T., Tison, J. L., Else, B., Thomas, H., et al. (2012). Dynamics of pCO2 and related air-ice CO2 fluxes in the Arctic coastal zone (Amundsen Gulf, Beaufort Sea). *Journal of Geophysical Research*, *117*, C00G10. https://doi.org/10.1029/2011JC00711

Geilfus, N. X., Galley, R. J., Crabeck, O., Papakyriakou, T., Landy, J., Tison, J. L., et al. (2015). Inorganic carbon dynamics of melt-pond-covered first-year sea ice in the Canadian Arctic. *Biogeosciences*, *12*(6), 2047–2061. https://doi.org/10.5194/bg-12-2047-2015

Gosink, T. A., Pearson, J. G., & Kelley, J. J. (1976). Gas movement through sea ice. *Nature*, *263*(5572), 41–42. https://doi.org/10.1038/263041a0

Hignett, P. (1998). *Correction of airborne SST measurements for blackness effects, MRF Tech. Note 28* (p. 15). Hampshire, England: Meteorol. Res. Flight.

Ho, D. T., Law, C. S., Smith, M. J., Schlosser, P., Harvey, M., & Hill, P. (2006). Measurements of air-sea gas exchange at high wind speeds in the Southern Ocean: Implications for global parameterizations. *Geophysical Research Letters*, *33*, L16611. https://doi.org/10.1029/2006GL026817

Honkanen, M., Tuovinen, J.-P., Laurila, T., Mäkelä, T., Hatakka, J., Kielosto, S., et al. (2018). Measuring turbulent CO_2 fluxes with a closed-path gas analyzer in a marine environment. *Atmospheric Measurement Techniques*, *11*(9), 5335–5350. https://doi.org/10.5194/amt-11-5335-2018

Hsieh, C.-I., Katul, G., & Chi, T. (2000). An approximate analytical model for footprint estimation of scalar fluxes in thermally stratified atmospheric flows. *Advances in Water Resources*, *23*(7), 765–772. https://doi.org/10.1016/s0309-1708(99)00042-1

Jähne, B., Münnich, K. O., Bösinger, R., Dutzi, A., Huber, W., & Libner, P. (1987). On the parameters influencing air-water gas exchange. *Journal of Geophysical Research*, *92*, 1937–1949. https://doi.org/10.1029/JC092iC02p01937

Kaimal, J. C., Izumi, Y., Wyngaard, J. C., & Cote, R. (1972). Spectral characteristics of surface-layer turbulence. *Quarterly Journal of the Royal Meteorological Society*, *98*(417), 563–589. https://doi.org/10.1002/qj.49709841707

Kljun, N., Calanca, P., Rotach, M. W., & Schmid, H. P. (2015). A simple two-dimensional parameterization for flux footprint prediction (FFP). *Geoscientific Model Development*, *8*(11), 3695–3713. https://doi.org/10.5194/gmd-8-3695-2015

Kormann, R., & Meixner, F. X. (2001). An analytical footprint model for non-neutral stratification. *Boundary-Layer Meteorology*, *99*(2), 207–224. https://doi.org/10.1023/a:1018991015119

Landwehr, S., Miller, S. D., Smith, M. J., Saltzman, E. S., & Ward, B. (2014). Analysis of the PKT correction for direct CO_2 flux measurements over the ocean. *Atmospheric Chemistry and Physics*, *14*(7), 3361–3372. https://doi.org/10.5194/acp-14-3361-2014

Loose, B., Kelly, R. P., Bigdeli, A., Williams, W., Krishfield, R., Rutgers van der Loeff, M., et al. (2017). How well does wind speed predict air-sea gas transfer in the sea ice zone? A synthesis of radon deficit profiles in the upper water column of the Arctic Ocean. *Journal of Geophysical Research: Oceans*, *122*(5), 3696–3714. https://doi.org/10.1002/2016jc012460

Loose, B., McGillis, W. R., Perovich, D., Zappa, C. J., & Schlosser, P. (2014). A parameter model of gas exchange for the seasonal sea ice zone. *Ocean Science*, *10*, 17–28. https://doi.org/10.5194/os-10-17-2014

Loose, B., McGillis, W. R., Schlosser, P., Perovich, D., & Takahashi, T. (2009). Effects of freezing, growth, and ice cover on gas transport processes in laboratory seawater experiments. *Geophysical Research Letters*, *36*, L05603. https://doi.org/10.1029/2008GL036318

Lovely, A., Loose, B., Schlosser, P., McGillis, W., Zappa, C., Perovich, D., et al. (2015). The Gas Transfer through Polar Sea ice experiment: Insights into the rates and pathways that determine geochemical fluxes. *Journal of Geophysical Research: Oceans*, *120*, 8177–8194. https://doi.org/10.1002/2014JC010607

Lüpkes, C., Gryanik, V. M., Hartmann, J., & Andreas, E. L. (2012), A parameterization, based on sea ice morphology, of the neutral atmospheric drag coefficients for weather prediction and climate models, *Journal of Geophysical Research*, *117*, D13112. https://doi.org/10.1029/2012jd017630

MacGilchrist, G. A., Naveira Garabato, A. C., Tsubouchi, T., Bacon, S., Torres-Valdés, S., & Azetsu-Scott, K. (2014). The Arctic Ocean carbon sink. *Deep Sea Research, Part. I*, *86*, 39–55. https://doi.org/10.1016/j.dsr.2014.01.002

MacIntyre, S., Fram, J. P., Kushner, P. J., Bettez, N. D., O'Brien, W. J., Hobbie, J. E., et al. (2009). Climate-related variations in mixing dynamics in an Alaskan arctic lake. *Limnology & Oceanography*, *54*(6p2), 2401–2417. https://doi.org/10.4319/lo.2009.54.6_part_2.2401

MacIntyre, S., Jonsson, A., Jansson, M., Aberg, J., Turney, D. E., & Miller, S. D. (2010). Buoyancy flux, turbulence, and the gas transfer coefficient in a stratified lake. *Geophysical Research Letters*, *37*, L24604. https://doi.org/10.1029/2010gl044164

Marcq, S., & Weiss, J. (2012). Influence of sea ice lead-width distribution on turbulent heat transfer between the ocean and the atmosphere. *The Cryosphere*, *6*(1), 143–156. https://doi.org/10.5194/tc-6-143-2012

McGillis, W. R., Edson, J. B., Hare, J. E., & Fairall, C. W. (2001). Direct covariance air-sea CO_2 fluxes. *Journal of Geophysical Research*, *106*, 16729–16745. https://doi.org/10.1029/2000JC000506

McKenna, S. P., & McGillis, W. R. (2004). The role of free-surface turbulence and surfactants in air-water gas transfer. *International Journal of Heat and Mass Transfer*, *47*, 539–553.

Miller, L. A., Carnat, G., Else, B. G. T., Sutherland, N., & Papakyriakou, T. N. (2011). Carbonate system evolution at the Arctic Ocean surface during autumn freeze-up. *Journal of Geophysical Research*, *116*. https://doi.org/10.1029/2011jc007143

Miller, L. A., Fripiat, F., Else, B. G. T., Bowman, J. S., Brown, K. A., Collins, R. E., et al. (2015). Methods for biogeochemical studies of sea ice: The state of the art, caveats, and recommendations. *Elementa: Science of The Anthropocene*, *3*, 38. https://doi.org/10.12952/journal.elementa.000038

Miller, S. D., Goulden, M. L., Menton, M. C., da Rocha, H. R., de Freitas, H. C., Figueira, A. M. e S., et al. (2004). Biometric and micrometeorological measurements of tropical forest carbon balance. *Ecological Applications*, *14*(sp4), 114–126. https://doi.org/10.1890/02-6005

Miller, S. D., Marandino, C., & Saltzman, E. S. (2010). Ship-based measurement of air-sea CO_2 exchange by eddy covariance. *Journal of Geophysical Research*, *115*, D02304. https://doi.org/10.1029/2009JD012193

Miller, L. A., Papakyriakou, T. N., Collins, R. E., Deming, J. W., Ehn, J. K., Macdonald, R. W., et al. (2011). Carbon dynamics in sea ice: A winter flux time series. *Journal of Geophysical Research*, *116*, C02028. https://doi.org/10.1029/2009JC006058

Nightingale, P. D., Malin, G., Law, C. S., Watson, A. J., Liss, P. S., Liddicoat, M. I., et al. (2000). In situ evaluation of air-sea gas exchange parameterizations using novel conservative and volatile tracers. *Global Biogeochemical Cycles*, *14*, 373–387. https://doi.org/10.1029/1999GB900091

Nomura, D., Granskog, M. A., Assmy, P., Simizu, D., & Hashida, G. (2013). Arctic and Antarctic sea ice acts as a sink for atmospheric CO_2 during periods of snowmelt and surface flooding. *Journal of Geophysical Research: Oceans*, *118*, 6511–6524. https://doi.org/10.1002/2013JC009048

Nomura, D., Granskog, M. A., Fransson, A., Chierici, M., Silyakova, A., Ohshima, K. I., et al. (2018). CO_2 flux over young and snow-covered Arctic pack ice in winter and spring. *Biogeosciences*, *15*(11), 3331–3343. https://doi.org/10.5194/bg-15-3331-2018

Nomura, D., Yoshikawa-Inoue, H., Toyota, T., & Shirasawa, K. (2010). Effects of snow, snow melting and refreezing processes on air–sea-ice CO_2 flux. *Journal of Glaciology*, *56*(196), 262–270. https://doi.org/10.3189/002214310791968548

Payne, R. E. (1972). Albedo of the sea surface. *Journal of the Atmospheric Sciences*, *29*(5), 959–970. https://doi.org/10.1175/1520-0469(1972)029<0959:aotss>2.0.co;2

Persson, P. O. G., Hare, J. E., Fairall, C. W., & Otto, W. D. (2005). Air–sea interaction processes in warm and cold sectors of extratropical cyclonic storms observed during FASTEX. *Quarterly Journal of the Royal Meteorological Society*, *131*(607), 877–912. https://doi.org/10.1256/qj.03.181

Prytherch, J., Brooks, I. M., Crill, P. M., Thornton, B. F., Salisbury, D. J., Tjernström, M., et al. (2017). Direct determination of the air-sea CO_2 gas transfer velocity in Arctic sea ice regions. *Geophysical Research Letters*, *44*, 3770–3778. https://doi.org/10.1002/2017GL073593

Prytherch, J., Yelland, M. J., Brooks, I. M., Tupman, D. J., Pascal, R. W., Moat, B. I., et al. (2015). Motion-correlated flow distortion and wave-induced biases in air-sea flux measurements from ships. *Atmospheric Chemistry and Physics*, *15*(18), 10619–10629. https://doi.org/10.5194/acp-15-10619-2015

Prytherch, J., Yelland, M. J., Pascal, R. W., Moat, B. I., Skjelvan, I., & Neill, C. C. (2010). Direct measurements of the CO_2 flux over the ocean: Development of a novel method. *Geophysical Research Letters*, *37*, L03607. https://doi.org/10.1029/2009GL041482

Read, J. S., Hamilton, D. P., Desai, A. R., Rose, K. C., MacIntyre, S., Lenters, J. D., et al. (2012). Lake-size dependency of wind shear and convection as controls on gas exchange. *Geophysical Research Letters*, *39*, L09405. https://doi.org/10.1029/2012gl051886

Rutgers van der Loeff, M. M., Cassar, N., Nicolaus, M., Rabe, B., & Stimac, I. (2014). The influence of sea ice cover on air-sea gas exchange estimated with radon-222 profiles. *Journal of Geophysical Research: Oceans*, *119*, 2735–2751. https://doi.org/10.1002/2013JC009321

Sabbaghzadeh, B., Upstill-Goddard, R. C., Beale, R., Pereira, R., & Nightingale, P. D. (2017). The Atlantic Ocean surface microlayer from 50°N to 50°S is ubiquitously enriched in surfactants at wind speeds up to 13m s^{-1}. *Geophysical Research Letters*, *44*, 2852–2858. https://doi.org/10.1002/2017GL072988

Salter, M. E., Upstill-Goddard, R. C., Nightingale, P. D., Archer, S. D., Blomquist, B., Ho, D. T., et al. (2011). Impact of an artificial surfactant release on air-sea gas fluxes during Deep Ocean Gas Exchange Experiment II. *Journal of Geophysical Research*, *116*, C11016. https://doi.org/10.1029/2011jc007023

Sievers, J., Sørensen, L. L., Papakyriakou, T., Else, B., Sejr, M. K., Haubjerg Søgaard, D., et al. (2015). Winter observations of CO_2 exchange between sea ice and the atmosphere in a coastal fjord environment. *The Cryosphere*, *9*(4), 1701–1713. https://doi.org/10.5194/tc-9-1701-2015

Smith, S. (1988). Coefficients for sea surface wind stress, heat flux, and wind profiles as a function of wind speed and temperature. *Journal of Geophysical Research*, *93*, 15467–15472. https://doi.org/10.1029/JC093iC12p15467

Spreen, G., Kaleschke, L., & Heygster, G. (2008). Sea ice remote sensing using AMSR-E 89-GHz channels. *Journal of Geophysical Research*, *113*, C02S03. https://doi.org/10.1029/2005JC003384

Takagi, K., Nomura, M., Ashiya, D., Takahashi, H., Sasa, K., Fujinuma, Y., et al. (2005). Dynamic carbon dioxide exchange through snowpack by wind-driven mass transfer in a conifer-broadleaf mixed forest in northernmost Japan. *Global Biogeochemical Cycles*, *19*, GB2012. https://doi.org/10.1029/2004gb002272

Takahashi, T., Sutherland, S. C., Wanninkhof, R., Sweeney, C., Feely, R. A., Chipman, D. W., et al. (2009). Climatological mean and decadal change in surface ocean pCO_2, and net sea–air CO_2 flux over the global oceans. *Deep Sea Research, Part. II*, *56*(8), 554–577. https://doi.org/10.1016/j.dsr2.2008.12.009

Tjernström, M., Birch, C. E., Brooks, I. M., Shupe, M. D., Persson, P. O. G., Sedlar, J., et al. (2012). Meteorological conditions in the central arctic summer during the arctic summer cloud ocean study (ASCOS). *Atmospheric Chemistry and Physics*, *12*(15), 6863–6889. https://doi.org/10.5194/acp-12-6863-2012

Vachon, D., & Prairie, Y. T. (2013). The ecosystem size and shape dependence of gas transfer velocity versus wind speed relationships in lakes. *Canadian Journal of Fisheries and Aquatic Sciences*, *70*(12), 1757–1764. https://doi.org/10.1139/cjfas-2013-0241

van Dijk, A., Moene, A. F., & de Bruin, H. (2004). *The principles of surface flux physics: Theory, practice and description of the ECPACK library*. Retrieved from www.met.wau.nl/projects/jep

Vesala, T., Kljun, N., Rannik, Ü., Rinne, J., Sogachev, A., Markkanen, T., et al. (2008). Flux and concentration footprint modelling: State of the art. *Environmental Pollution*, *152*(3), 653–666. https://doi.org/10.1016/j.envpol.2007.06.070

Vickers, D., & Mahrt, L. (1997). Quality control and flux sampling problems for tower and aircraft data. *Journal of Atmospheric and Oceanic Technology*, *14*(3), 512–526. https://doi.org/10.1175/1520-0426(1997)014<0512:qcafsp>2.0.co

Wanninkhof, R. (1992). Relationship between wind speed and gas exchange over the ocean. *Journal of Geophysical Research*, *97*(C5), 7373. https://doi.org/10.1029/92jc00188

Wanninkhof, R. (2014). Relationship between wind speed and gas exchange over the ocean revisited. *Limnology and Oceanography: Methods*, *12*(6), 351–362. https://doi.org/10.4319/lom.2014.12.351

Wanninkhof, R., Asher, W. E., Ho, D. T., Sweeney, C., & McGillis, W. R. (2009). Advances in quantifying air-sea gas exchange and environmental forcing. *Annual Review of Marine Science*, *1*, 213–244. https://doi.org/10.1146/annurev.marine.010908.163742

Webb, E. K., Pearman, G. I., & Leuning, R. (1980). Correction of flux measurements for density effects due to heat and water vapor transfer. *Quarterly Journal of the Royal Meteorological Society*, *106*(447), 85–100. https://doi.org/10.1002/qj.49710644707

Weiss, R. (1974). Carbon dioxide in water and seawater: The solubility of a non-ideal gas. *Marine Chemistry*, *2*(3), 203–215. https://doi.org/10.1016/0304-4203(74)90015-2

Wernecke, A., & Kaleschke, L. (2015). Lead detection in arctic sea ice from CryoSat-2: Quality assessment, lead area fraction and width distribution. *The Cryosphere*, *9*(5), 1955–1968. https://doi.org/10.5194/tc-9-1955-2015

Wilczak, J. M., Oncley, S. P., & Stage, S. A. (2001). Sonic anemometer tilt correction algorithms. *Boundary-Layer Meteorology*, *99*(1), 127–150. https://doi.org/10.1023/a:1018966204465

Woolf, D. K. (2005). Parameterization of gas transfer velocities and sea-state-dependent wave breaking. *Tellus B: Chemical and Physical Meterology*, *57*, 87–94. https://doi.org/10.1111/j.1600-0889.2005.00139.x

Woolf, D. K., Shutler, J. D., Goddijn-Murphy, L., Watson, A. J., Chapron, B., Nightingale, P. D., et al. (2019). Key uncertainties in the recent air-sea flux of CO_2. *Global Biogeochemical Cycles*, *33*(12), 1548–1563. https://doi.org/10.1029/2018gb006041

Yang, M., Prytherch, J., Kozlova, E., Yelland, M. J., Parenkat Mony, D., & Bell, T. G. (2016). Comparison of two closed-path cavity-based spectrometers for measuring air-water CO_2 and CH_4 fluxes by eddy covariance. *Atmospheric Measurement Technique*, *9*(11), 5509–5522. https://doi.org/10.5194/amt-9-5509-2016

Yasunaka, S., Siswanto, E., Olsen, A., Hoppema, M., Watanabe, E., Fransson, A., et al. (2018). Arctic Ocean CO_2 uptake: An improved multiyear estimate of the air-sea CO_2 flux incorporating chlorophyll a concentrations. *Biogeosciences*, *15*(6), 1643–1661. https://doi.org/10.5194/bg-15-1643-2018

Yelland, M. J., Moat, B. I., Pascal, R. W., & Berry, D. I. (2002). CFD model estimates of the airflow distortion over research ships and the impact on momentum flux measurements. *Journal of Atmospheric and Oceanic Technology*, *19*, 1477–1499. https://doi.org/10.1175/1520-0426(2002)019<1477:CMEOTA>2.0.CO;2

Zippel, S., & Thomson, J. (2016). Air-sea interactions in the marginal ice zone. *Elementa: Science of The Anthropocene*, *4*(1), 95. https://doi.org/10.12952/journal.elementa.000095

References From the Supporting Information

Bariteau, L., Helmig, D., Fairall, C. W., Hare, J. E., Hueber, J., & Lang, E. K. (2010). Determination of oceanic ozone deposition by ship-borne eddy covariance flux measurements. *Atmospheric Measurement Techniques*, *3*(2), 441–455. https://doi.org/10.5194/amt-3-441-2010

Horst, T. W. (1997). A simple formula for attenuation of eddy fluxes measured with first-order-response scalar sensors. *Boundary-Layer Meteorology*, *82*(2), 219–233. https://doi.org/10.1023/a:1000229130034

Massman, W. J., & Clement, R. (2004). Uncertainty in eddy covariance flux estimates resulting from spectral attenuation. In X. Lee, W. J. Massman, & B. E. Law (Eds.), *Handbook of micrometeorology, A guide for surface flux measurement and analysis* (pp. 67–99). Kluwer Dordrecht, Netherlands: Springer.

Moncrieff, J. B., Massheder, J. M., de Bruin, H., Elbers, J., Friborg, T., Heusinkveld, B., et al. (1997). A system to measure surface fluxes of momentum, sensible heat, water vapor and carbon dioxide. *Journal of Hydrology*, *188–189*, 589–611. https://doi.org/10.1016/s0022-1694(96)03194-0

Spirig, C., Neftel, A., Ammann, C., Dommen, J., Grabmer, W., Thielmann, A., et al. (2005). Eddy covariance flux measurements of biogenic VOCs during ECHO 2003 using proton transfer reaction mass spectrometry. *Atmospheric Chemistry and Physics*, *5*(2), 465–481. https://doi.org/10.5194/acp-5-465-2005